Identifying Signatures of Natural Climate Variability in Time Series of Global-Mean Surface Temperature: Methodology and Insights

DAVID W. J. THOMPSON

Department of Atmospheric Science, Colorado State University, Fort Collins, Colorado

JOHN M. WALLACE

Department of Atmospheric Sciences, University of Washington, Seattle, Washington

PHIL D. JONES

Climatic Research Unit, University of East Anglia, Norwich, United Kingdom

JOHN J. KENNEDY

Met Office Hadley Centre, Exeter, United Kingdom

(Manuscript received 11 February 2009, in final form 23 May 2009)

ABSTRACT

Global-mean surface temperature is affected by both natural variability and anthropogenic forcing. This study is concerned with identifying and removing from global-mean temperatures the signatures of natural climate variability over the period January 1900–March 2009. A series of simple, physically based methodologies are developed and applied to isolate the climate impacts of three known sources of natural variability: the El Niño–Southern Oscillation (ENSO), variations in the advection of marine air masses over the high-latitude continents during winter, and aerosols injected into the stratosphere by explosive volcanic eruptions. After the effects of ENSO and high-latitude temperature advection are removed from the global-mean temperature record, the signatures of volcanic eruptions and changes in instrumentation become more clearly apparent. After the volcanic eruptions are subsequently filtered from the record, the residual time series reveals a nearly monotonic global warming pattern since ~1950. The results also reveal coupling between the land and ocean areas on the interannual time scale that transcends the effects of ENSO and volcanic eruptions. Globally averaged land and ocean temperatures are most strongly correlated when ocean leads land by ~2–3 months. These coupled fluctuations exhibit a complicated spatial signature with largest-amplitude sea surface temperature perturbations over the Atlantic Ocean.

1. Introduction

The time history of observed twentieth-century global-mean surface temperature reflects the combined influences of naturally occurring climate variations and anthropogenic emissions of greenhouse gases and sulfate aerosols. A technique used extensively in the Intergovernmental Panel on Climate Change (IPCC) assessment reports for distinguishing the signal of an-

thropogenic forcing from natural variability involves comparing (a) the observed spatial signature of climate change with (b) the signature of anthropogenic climate change inferred from climate models forced with prescribed increasing greenhouse gas concentrations [i.e., the ''optimal fingerprinting'' technique; Hegerl et al. (2007) and references therein]. Here, we infer the anthropogenic signal and other key aspects of twentieth-century global-mean surface temperature variability by subtracting from the observed global-mean land and ocean temperature records the variance associated with known sources of natural climate variability.

Previous studies have estimated the variance in global-mean temperature attributable to natural climate

Corresponding author address: David W. J. Thompson, Dept. of Atmospheric Science, Colorado State University, Fort Collins, CO 80523.
E-mail: davet@atmos.colostate.edu

variability but have relied largely on statistical fits to prescribed climate indices. The signal of the El Niño–Southern Oscillation (ENSO) in global surface temperatures has been estimated using linear regression based on lagged indices of the Southern Oscillation index or equatorial Pacific sea surface temperatures (e.g., Jones 1988; Mass and Portman 1989; Robock and Mao 1995; Kelly and Jones 1996; Wigley 2000; Santer et al. 2001; Trenberth et al. 2002), maximum covariance analysis between surface temperatures in the tropical Pacific and over the continents (Yang and Schlesinger 2001), complex "patterns-based filters" derived from linear inverse models (Penland and Matrosova 2006; Compo and Sardeshmukh 2008, manuscript submitted to *J. Climate*), and regression analyses with geographically dependent lag (Chen et al. 2008). The signal of volcanic eruptions has been prescribed as linear cooling followed by exponential warming (Wigley 2000; Santer et al. 2001).

In this study we exploit a series of novel methodologies to identify and filter out of the unsmoothed monthly mean time series of global-mean land and ocean temperatures the variance associated with ENSO, dynamically induced atmospheric variability, and volcanic eruptions. The impacts of ENSO and volcanic eruptions on global-mean temperature are estimated using a simple thermodynamic model of the global atmospheric–oceanic mixed layer response to anomalous heating. In the case of ENSO, the heating is assumed to be proportional to the sea surface temperature anomalies over the eastern Pacific; in the case of volcanic eruptions, the heating is assumed to be proportional to the stratospheric aerosol loading. The impacts of dynamically induced atmospheric variability on global-mean temperature are estimated on the basis of the covariance between the land–sea temperature difference in the Northern Hemisphere and the sea level pressure field. The filtering methodology reduces the high-frequency variability in global-mean temperatures not by smoothing the data, but rather by subtracting out physically based estimates of the time-dependent signatures of known sources of natural climate variability. Hence, the resulting residual global-mean temperature time series has the same monthly time resolution as does the original data.

The results of the filtering process provide several new insights into twentieth-century global-mean temperature variability. After ENSO and the dynamically induced variability are removed from global-mean temperatures, the residual time series highlights a spurious drop in SSTs in 1945 and sharpens substantially the signal of major volcanic eruptions in surface temperatures. After the signature of the volcanic eruptions is removed, the residual global-mean temperature time series exhibits nearly monotonic warming since ~1950. The results also 1) reveal a significant level of coupling between ocean and land temperatures that remains even after the effects of ENSO and volcanic eruptions have been removed; 2) serve to highlight the improvements in the quality of the time series of global-mean land temperatures with the increase in the areal coverage of the station network from 1951 onward; and 3) yield a residual time series in which the signature of anthropogenically induced global warming is more prominent.

The paper is organized as follows: In section 2 we provide a brief review of the data used in the analysis. In section 3 we describe the methodologies used to remove from the global-mean temperature time series the impacts of ENSO and dynamically induced variability. In section 4 we examine the signal of volcanic eruptions in the residual time series from which the effects of ENSO and dynamically induced variability have been removed. Section 5 describes the methodology used to remove the impacts of volcanic eruptions from the global-mean temperature time series, and section 6 discusses key aspects of global-mean temperature variability highlighted by the residual time series. Section 7 provides a summary of the key results.

2. Data and analysis details

The temperature data used in the study are version 3 of the Climate Research Unit's land surface air temperature dataset (CRUTEM3; Brohan et al. 2006), version 2 of the Hadley Centre's Sea Surface Temperature dataset (HadSST2; Rayner et al. 2006), and version 3 of the Hadley Centre–Climate Research Unit's combined land surface temperature and SST dataset (HadCRUT3; Brohan et al. 2006). All temperature datasets are available from the Climatic Research Unit at the University of East Anglia in monthly mean form on a $5° \times 5°$ latitude–longitude mesh and are expressed as anomalies with respect to the 1961–90 base period. The sea level pressure (SLP) data are provided by the National Center for Atmospheric Research's Data Support Section and are also formatted as monthly means on a $5° \times 5°$ latitude–longitude mesh, as described in Trenberth and Paolino (1980). The seasonal cycle is removed from the SLP data by subtracting the long-term mean calculated for the period 1950–2006 from the data as a function of calendar month.

Time series are shown for the period January 1900–March 2009. Unless otherwise noted, all analyses performed in developing the filtering algorithms (including correlations and regressions) are based on detrended data limited to the period January 1950–December 2006 and are thus unaffected by the discontinuity in sea

surface temperatures in 1945 described by Thompson et al. (2008). Detrending ensures that the algorithms are not biased by the global warming of the past few decades. The effective sample size used in significance estimates is given by Eq. (31) in Bretherton et al. (1999).

The fitted and residual time series generated in the analyses outlined here are available online (www.atmos. colostate.edu/~davet/ThompsonWallaceJonesKennedy).

3. Removing the signatures of ENSO and dynamically induced variability from global-mean temperatures

a. Estimating the signal of ENSO in global-mean temperatures

As noted in the introduction, previous studies have defined the ENSO signal in the global-mean temperature record on the basis of lagged values of the east–west SLP gradient in the tropical Pacific (e.g., the Southern Oscillation index), or lagged values of SSTs averaged over the eastern tropical Pacific cold-tongue region (e.g., the "cold-tongue index" or Niño-3.4). Here, we define the ENSO signal as being linearly proportional to the damped thermodynamic response of the global atmospheric–oceanic mixed layer to the SST variability and associated surface heat fluxes in the eastern equatorial Pacific cold-tongue region. We focus on the response to variability only in the cold-tongue region for the following reasons: 1) the ENSO signal in global-mean temperature is derived primarily from the exchange of heat between the subsurface ocean and the global atmospheric–oceanic mixed layer, 2) ENSO primarily perturbs the flux of heat between the subsurface ocean and the global atmospheric–oceanic mixed layer in the region of ocean upwelling in the eastern equatorial Pacific, and 3) SST anomalies outside the cold-tongue region exhibit considerable decadal variability, much of which is not linked to ENSO dynamics.

The approach is analogous to that exploited by Hasselman (1976) to examine the ocean response to stochastic atmospheric forcing, and by Yulaeva and Wallace (1994) to examine the tropical-mean response to ENSO. The global-mean surface temperature response to variability in ENSO is modeled as

$$C \frac{d}{dt} T_{\text{ENSO}}(t) = F(t) - \frac{T_{\text{ENSO}}(t)}{\beta}, \quad (1)$$

where T_{ENSO} denotes the simulated response of global-mean surface temperatures to ENSO variability, $F(t)$ is the anomalous flux of sensible and latent heat in the eastern tropical Pacific, β is a linear damping coefficient, and C is the effective heat capacity of the global atmospheric–oceanic mixed layer per unit area.

The anomalous heat fluxes given by $F(t)$ are assumed to be linearly congruent with variability in sea surface temperatures in the dynamically active cold-tongue region. That is, the ocean dynamics force variability in sea surface temperatures in the cold tongue, and this variability is communicated to the atmosphere via the anomalous fluxes of heat at the ocean surface. The heat fluxes are estimated by 1) subtracting monthly mean SST anomalies averaged over the globe from SST anomalies averaged over the dynamically active cold-tongue region to form the *difference* cold-tongue index (CTI; the cold-tongue region is defined as 5°N–5°S, 180°–90°W) and 2) multiplying the *difference* CTI time series by (a) the fractional area of the globe covered by the cold-tongue region (assumed to be 2%) and (b) a coupling coefficient of 10 W m^{-2} K^{-1} (cf. Fig. 17 from Barnett et al. 1991).

The linear damping coefficient β is a measure of the climate sensitivity. Observationally and numerically derived estimates of β range from ~0.4 to 1.2 K (W m^{-2})$^{-1}$ and the value of β depends on both the time scale and nature of the forcing (e.g., Cess 1976; Hansen et al. 1985; Forster and Gregory 2006; Knutti et al. 2008; Solomon et al. 2007). Here, we set β to ⅔ K (W m^{-2})$^{-1}$. In practice, the results are not sensitive to the choice of the air–sea coupling coefficient or β provided that the values fall within the range that is physically reasonable.

The effective heat capacity of the model was determined empirically so that the correlation coefficient between T_{ENSO} and the time series of global-mean surface temperature anomalies is maximized based on detrended data from 1950 through 2006. The optimal effective heat capacity ($C \sim 1.84 \times 10^7$ J m^{-2} K^{-1}) implies that the ENSO-related heat fluxes warm the entire atmosphere plus an equivalent of ~2 m of the global ocean. Note that the resulting heat capacity is a global average and that, locally, ENSO perturbs the oceanic mixed layer much deeper than ~2 m. The model was initialized with anomalies in the cold-tongue region starting in 1870 and the output T_{ENSO} was retained for the period January 1900–March 2009.

The difference cold-tongue index and the output of Eq. (1) (T_{ENSO}) are shown in the top panel of Fig. 1. The simple thermodynamic model acts to low-pass filter the input series and lag it by several months. The output time series yields a substantially improved representation of the signal of ENSO in global-mean temperatures: the global-mean temperature time series is more strongly correlated with T_{ENSO} than with the difference cold-tongue index ($r = 0.41$ versus $r = 0.31$). We will show the residual time series obtained by subtracting the T_{ENSO} time series from the global-mean temperature time series later in this section.

a) Time series of ENSO

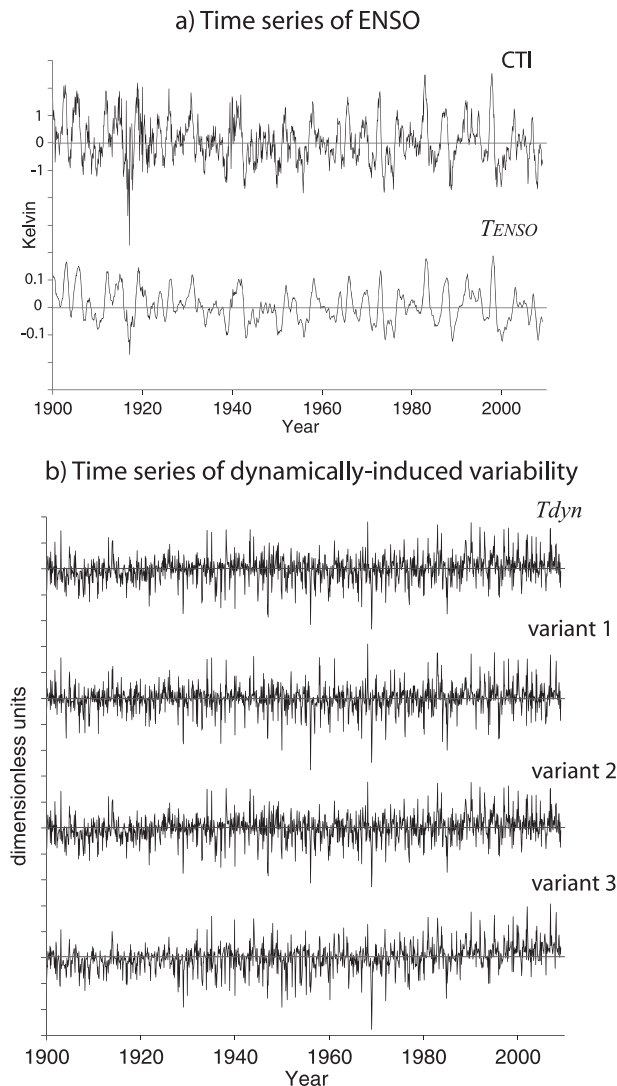## b) Time series of dynamically-induced variability

FIG. 1. (a, top) Time series of SST anomalies in the eastern tropical Pacific used to drive Eq. (1) (i.e., the CTI), and (a, bottom) the output of Eq. (1) (T_{ENSO}). Tick marks are 1 K for the CTI and 0.1 K for T_{ENSO}. (b) Time series of the contribution of dynamically induced variability to global-mean temperatures. (top) The T_{dyn} time series found as the expansion coefficient time series of SLP regressed on $T_{NHLand-NHSST}$. (second from top) The linear sum of the first 10 PCs of the NH SLP field, where the PCs are weighted by the regression coefficient with $T_{NHLand-NHSST}$. (second from bottom) The expansion coefficient time series of SLP regressed on high-pass values of $T_{NHLand-NHSST}$. (bottom) The expansion coefficient time series of surface temperature regressed on $T_{NHLand-NHSST}$. See text for details of the calculations. All subsequent analyses are based on the top T_{dyn} time series.

b. Estimating the signal of dynamically induced variability in global-mean temperatures

Temporal variations in the atmospheric circulation contribute to the variability of global-mean temperatures

because of the large differences between the heat capacities of the ocean and land areas. For example, winter months when the surface westerlies are stronger than normal over middle and subpolar latitudes of the Northern Hemisphere (NH) are marked by anomalously strong warm advection over the NH continents and anomalously strong cold advection over the oceans. Since the land surface has a lower heat capacity than the oceanic mixed layer, the resulting temperature anomalies tend to be larger over the continents than over the ocean areas so that the global-mean temperature tends to be anomalously high, and vice versa. The impacts of dynamically induced variability on surface temperatures are most pronounced in the NH where the land areas account for a substantial fraction of the hemisphere, and during the winter season when the surface winds and the land–sea contrast in surface temperatures are largest.

Previous studies have estimated the impacts of dynamically induced variability on area-averaged temperatures using two somewhat different approaches. The first approximates the dynamically induced contribution to global-mean temperatures on the basis of preferred patterns of internal atmospheric variability. For example, the Northern Annular mode–North Atlantic Oscillation (NAM–NAO) accounts for a component of the dynamically induced variability in NH-mean temperatures by virtue of its strong influence on temperature over Eurasia and North America (e.g., Hurrell 1996; Thompson et al. 2000). The second method approximates the dynamically induced contribution to variations in global-mean temperatures on the basis of the cold-ocean–warm-land pattern (the COWL pattern; Wallace et al. 1995). The COWL pattern is defined by regressing the *departure* surface temperature field onto the time series of NH mean temperature, where the departure field is defined as the spatially varying temperature minus the NH mean. By construction, the expansion coefficient time series of the COWL pattern explains more variance of NH-mean temperatures than the time series associated with any other surface temperature pattern with a spatial mean of zero.

There are disadvantages to both of the above methods. The NAM–NAO is an important pattern of internal atmospheric dynamics, but is not necessarily the most important structure in terms of driving dynamically induced variability in hemispheric and global-mean temperatures. The COWL pattern explains a substantial fraction of the month-to-month variability in hemispheric and global-mean temperatures (Wallace et al. 1995), but the COWL pattern projects onto the predicted surface temperature response to greenhouse-induced warming and hence includes a component of the radiative response to increasing greenhouse gases (Broccoli et al. 1998).

Here, we estimate the contribution of dynamically induced variability to variations in global-mean temperature by adapting the COWL methodology to the SLP field. The resulting SLP pattern is not restricted to patterns of internal atmospheric variability, and it does not project onto the radiative response to increased carbon dioxide. The corresponding estimate of dynamically induced variability includes an anthropogenic component only to the extent that anthropogenic forcing drives large-scale changes in the Northern Hemisphere SLP field.

The analysis is performed as follows. First, we find the pattern in NH sea level pressure anomalies most strongly coupled to the difference between temperatures averaged over the NH land and ocean areas poleward of 30°N. The pattern is found by regressing SLP anomalies onto the land–ocean difference time series (hereafter $T_{\text{NHLand-NHSST}}$) rather than NH mean temperature since we are interested in isolating the pattern in SLP that contributes most to out-of-phase variations between the land and ocean areas. The $T_{\text{NHLand-NHSST}}$ basis index is detrended before calculating the regression coefficients and the analysis is restricted to the NH since land accounts for a relatively small fraction of the SH. The SLP maps are found for 3-month seasons centered on all calendar months so that the resulting patterns can vary from one season to the next (e.g., the SLP map for January is based on monthly mean data for the months December–February, the map for February on data for the months January–March, etc.). The analysis is based on the period 1950–2006.

The SLP loadings are found as

$$A(x, M) = \overline{\text{SLP}(x,t) \cdot \frac{T_{\text{NHLand-NHSST}}(t)}{\sigma_{T(t)}}}, \qquad (2)$$

where A denotes the regression coefficients given as a function of grid point x and calendar month M (e.g., February corresponds to $M = 2$); SLP denotes the SLP data; t corresponds to months $M - 1$, M, and $M + 1$ for all years 1950–2006; $T_{\text{NHLand-NHSST}}(t)/\sigma_{T(t)}$ denotes the detrended $T_{\text{NHLand-NHSST}}$ surface temperature time series for months t divided by its standard deviation; and the overbar denotes the time mean.

The patterns derived from Eq. (2) are summarized in the top panels in Fig. 2. The contours in the top panels in Fig. 2 show the $A(x, M)$ regression maps averaged over the cold (left) and warm (right) season months. The patterns are similar during the two seasons, but the centers of action are lower in amplitude and shifted poleward during summer. The wintertime SLP pattern bears resemblance to the signature of internal atmospheric variability in the North Pacific sector (i.e., it resembles the Pacific–North America pattern), but differs from the

pattern of the NAM–NAO over the Eurasian sector; that is, whereas the center of action of the NAM–NAO is focused over the Arctic and North Atlantic, the Eurasian center of action in the top panels of Fig. 2 is located farther to the east, along the Russian Arctic coast. The peculiar shape of the SLP pattern can be understood by superposing it on the climatological mean surface temperature pattern, indicated by the shading in the top panels of Fig. 2, which is derived from the National Centers for Environmental Prediction–National Center for Atmospheric Research (NCEP–NCAR) reanalysis data. During both seasons, the SLP pattern is situated so that the inferred geostrophic flow is oriented perpendicular to the climatological-mean temperature gradients over large areas of western North America and Russia. The SLP patterns are thus situated to maximize the anomalous temperature advection over the continents.

The expansion coefficient time series of the seasonally varying SLP patterns found in Eq. (2) is found by projecting the SLP data for all months onto the respective regression map (i.e., the time series for January is found by projecting the January SLP data onto the January regression map, etc.). Hence for calendar month M, the expansion coefficient time series is found to be

$$T_{\text{dyn}}(t) = \left[\text{SLP}(x,t)\frac{A(x)}{\sigma_{A(x)}}\right], \qquad (3)$$

where $\text{SLP}(x, t)$ denotes the anomalous SLP field for calendar month M; $A(x)$ is the SLP pattern for month M, as found in Eq. (2); $\sigma_{A(x)}$ denotes the (cosine weighted) spatial standard deviation of $A(x)$ for month M; and the brackets denote the (cosine weighted) spatial average over the NH poleward of 40°N. The regression maps $A(x)$ are standardized by $\sigma_{A(x)}$ separately for each calendar month since the seasonally varying amplitude of the SLP data is contained in $\text{SLP}(x, t)$ [i.e., if $A(x)$ were not standardized as a function of calendar month, then the seasonally varying amplitude in the SLP data would be weighted twice in the projection]. The time series for each month are concatenated to form a single expansion coefficient time series.

By construction, the expansion coefficient time series generated in Eq. (3) (hereafter labeled T_{dyn}) is more strongly correlated with variations in $T_{\text{NHLand-NHSST}}$ than the expansion coefficient time series associated with any other pattern in the SLP field. The correlation between T_{dyn} and $T_{\text{NHLand-NHSST}}$ calculated for all months in the detrended data between 1950 and 2006 is $r = 0.72$.

We examined whether other patterns in the SLP field contribute to $T_{\text{NHLand-NHSST}}$ by repeating the analysis in Eqs. (2) and (3), but for the case where the T_{dyn} index is linearly regressed from $T_{\text{NHLand-NHSST}}$ before

Patterns associated with *Tdyn*
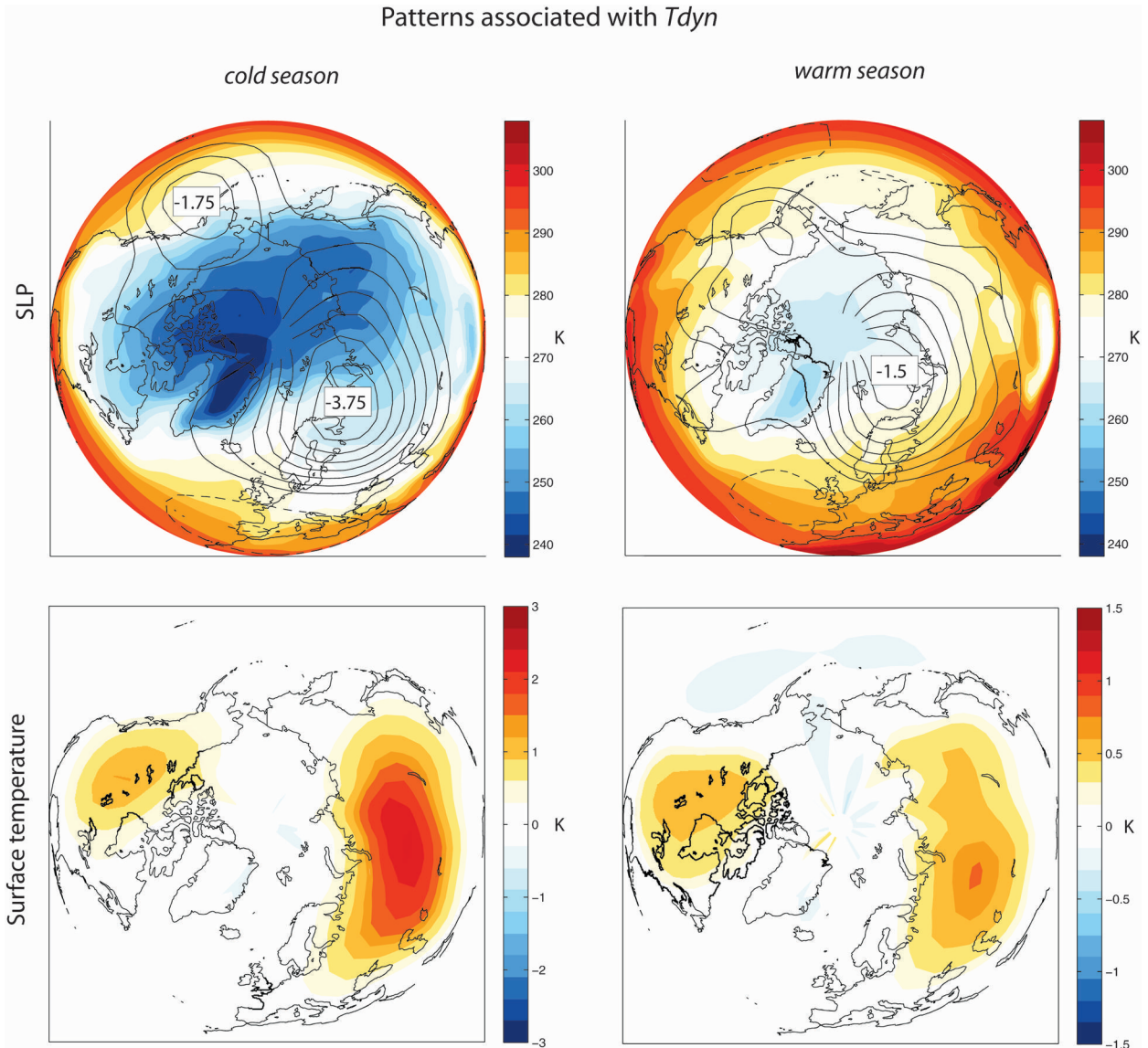
cold season

warm season

FIG. 2. Patterns formed by regressing SLP and surface temperature onto the time series of the difference between NH mean land and ocean temperatures ($T_{\text{NHLand-NHSST}}$). (top) The regression coefficients for SLP (contours) superposed on the climatological mean isotherms (shading). (bottom) The regression coefficients for surface temperature. (left) The results averaged over the cold season months (October–March). (right) The results averaged over the warm season months (April–September). Contour intervals are 0.5 and 0.2 hPa for the cold and warm seasons, respectively. Solid contours denote negative SLP anomalies; minima are labeled in hPa.

calculating $A(x)$. The resulting SLP pattern (not shown) is more polar-centric than that shown in Fig. 2 and its associated expansion coefficient is not correlated with $T_{\text{NHLand-NHSST}}$ ($r = 0.02$).

The efficiency of T_{dyn} in capturing the covariability between the SLP field and $T_{\text{NHLand-NHSST}}$ is exemplified by Fig. 3. The solid horizontal line corresponds to the correlation between $T_{\text{NHLand-NHSST}}$ and T_{dyn} ($r = 0.72$). The circles show the cumulative correlations between $T_{\text{NHLand-NHSST}}$ and the principal component (PC) time series of the NH (30°–90°N) SLP field. The PCs are

calculated as a function of calendar month, and the correlation associated with PC n denotes the cumulative correlation between $T_{\text{NHLand-NHSST}}$ and principal component time series $1 \rightarrow n$ (the total correlation is found as the square root of the sum of the squares of the correlations). As is evident in Fig. 3, T_{dyn} explains as much variance in $T_{\text{NHLand-NHSST}}$ as the first ~6 PC time series of the SLP field, and higher-order PC time series contribute little additional information to the correlation.

Figure 1b documents the T_{dyn} index time series and compares it with variants of the methodology outlined
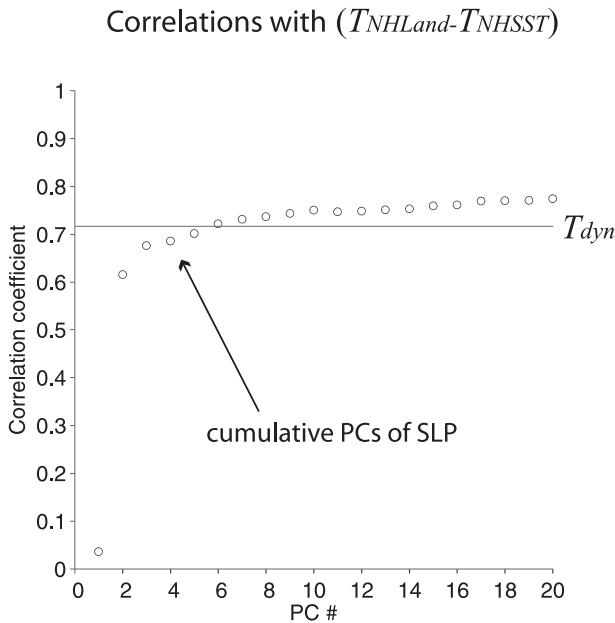
Correlations with (T_{NHLand}-T_{NHSST})

FIG. 3. Cumulative correlations (circles) between the leading PC time series of the NH SLP field and the $T_{\mathrm{NHLand\text{-}NHSST}}$ temperature time series. For example, the correlation for PC 3 denotes the total correlation between PCs 1–3 and $T_{\mathrm{NHLand\text{-}NHSST}}$. The horizontal line denotes the correlation between T_{dyn} and $T_{\mathrm{NHLand\text{-}NHSST}}$. Results based on monthly mean data 1950–2006.

above. The top time series shows the T_{dyn} index extended back to 1900 using the projection given by Eq. (3). The extended T_{dyn} index is dominated by variability on month-to-month time scales but also exhibits weak decadal variability consistent with trends toward falling SLP over the Arctic through the mid-1990s (e.g., Hurrell 1995; Thompson et al. 2000). The decadal variability in T_{dyn} is contained entirely in the SLP field. Hence, while T_{dyn} may reflect the effects of increasing greenhouse gases and/or decreasing stratospheric ozone, it does so only to the extent that such forcing is manifested in the variability of the atmospheric circulation.

The time series labeled variant 1 in Fig. 1b shows the linear combination of the leading 10 PCs of the SLP field (i.e., the PC time series used to generate the correlations in Fig. 3). In the summation, the individual PCs are weighted by their respective regression coefficients with $T_{\mathrm{NHLand\text{-}NHSST}}$. The resulting combined PC time series is largely indistinguishable from T_{dyn} (cf. the top two time series in Fig. 1b), and the correlation between the time series for the period 1950–2006 is $r = 0.88$.

The time series labeled variant 2 examines the impacts of decadal variability in the temperature field on the development of the T_{dyn} index. In this case, the fifth-order polynomial fit is removed from $T_{\mathrm{NHLand\text{-}NHSST}}$ before calculating the SLP patterns in Eq. (2). The resulting SLP patterns (not shown) are virtually identical

to those derived from the unfiltered $T_{\mathrm{NHLand\text{-}NHSST}}$ time series, and the associated expansion coefficient time series (third from top time series in Fig. 1, bottom panel) exhibits decadal variability comparable to that found in T_{dyn}. The correlation between T_{dyn} and the third from the top time series is $r = 0.99$.

The time series labeled variant 3 shows results derived by replacing the gridded SLP data in Eqs. (2) and (3) with gridded surface temperature data. The corresponding cold and warm season regression maps are shown in the bottom panels of Fig. 2. The regression maps are physically consistent with the patterns of temperature advection inferred by the SLP patterns in the top panels of Fig. 2; that is, temperatures are warmest in regions of warm advection. Note that the cold season surface temperature pattern in the bottom panels of Fig. 2 is analogous to the COWL pattern found in Wallace et al. (1995), but is based on regressions, not onto the hemispheric mean temperature, but rather onto the difference time series given by $T_{\mathrm{NHLand\text{-}NHSST}}$.

The expansion coefficient time series for the temperature-based results is found using the projection in Eq. (3) (except that the SLP data are replaced with the surface temperature data). The resulting time series (variant 3 in Fig. 1b) is highly correlated with $T_{\mathrm{NHLand\text{-}NHSST}}$ ($r = 0.91$) and exhibits a marked trend over the past few decades, consistent with the enhanced warming of the land areas relative to the ocean areas since ~1980. The high correlation ($r = 0.91$) between $T_{\mathrm{NHLand\text{-}NHSST}}$ and variant 3 reveals that the temperature field is more efficient than the SLP field in explaining variability in $T_{\mathrm{NHLand\text{-}NHSST}}$, particularly on month-to-month time scales. However, the low-frequency variability in variant 3 is likely impacted by the thermodynamic surface response to greenhouse gas forcing. For this reason, we view the index based on the SLP field as being a more reliable estimate of the impacts of atmospheric dynamics on surface temperatures.

c. Removing the effects of ENSO and dynamically induced variability from global-mean temperatures

The T_{ENSO} and SLP-based T_{dyn} index time series derived in the previous sections are removed from three global-mean temperature time series: the combined global-mean land and ocean time series (hereafter T_g), the global-mean land time series (T_{Land}), and the global-mean ocean time series (T_{SST}).

The components of the global-mean time series that are linearly congruent with T_{ENSO} and T_{dyn} are given by

$$x_{\mathrm{fitted}}(t) = \alpha \cdot x(t) \quad \text{where} \quad \alpha = \frac{\overline{x'(t) \cdot T'(t)}}{\overline{x'^2(t)}}, \quad (4)$$
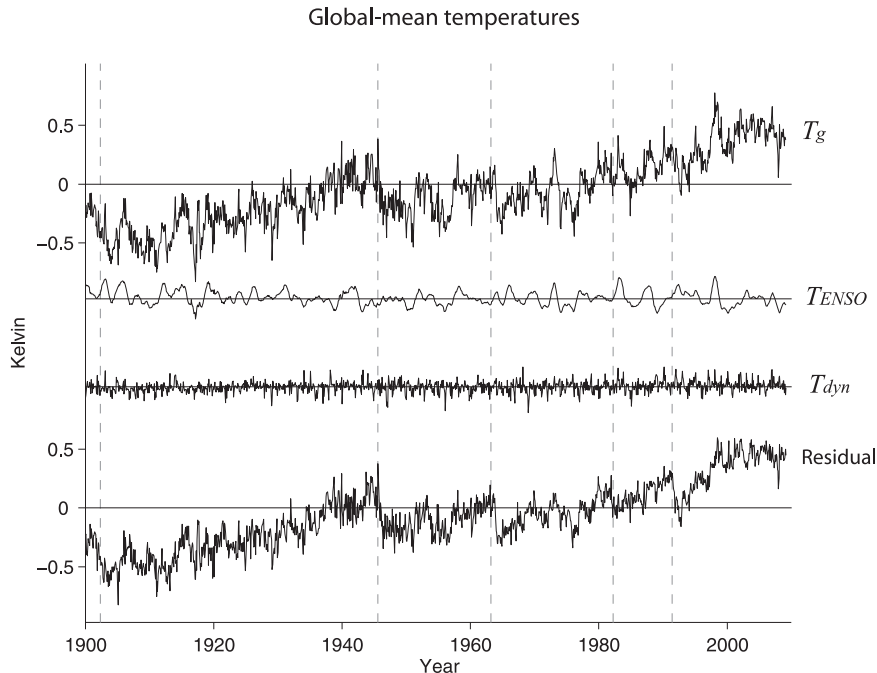
FIG. 4. (top) The time series of global-mean, monthly mean surface temperature anomalies based on the HadCRUT3 combined SST and land surface air temperature data (T_g). (second from top) The component of T_g that is linearly congruent with T_{ENSO}. (second from bottom) The component of T_g that is linearly congruent with T_{dyn}. (bottom) The residual global-mean surface temperature time series found by removing the linear contributions of T_{ENSO} and T_{dyn} from T_g. The vertical lines denote the month of August 1945 and volcano eruption dates (from left to right) of Santa María, Mount Agung, El Chichón, and Mount Pinatubo. The horizontal lines denote the mean for the period 1961–90 (i.e., the base period for the temperature data).

in which the overbars denote the long-term mean, primes denote departures from the long-term mean, $T(t)$ denotes the respective global-mean temperature time series, $x(t)$ denotes the T_{ENSO} or T_{dyn} index time series, α corresponds to the regression of $x(t)$ onto $T(t)$, and $x_{fitted}(t)$ corresponds to the component of $T(t)$ that is linearly congruent with variations in T_{ENSO} or T_{dyn}. The regression coefficients (α) are calculated for detrended monthly mean data for 1950–2006 and are calculated separately for T_{ENSO} and T_{dyn} since the time series are effectively uncorrelated ($r = 0.03$). Note also that the signal of dynamically induced variability is not filtered from the ocean time series since T_{dyn} and T_{SST} are not correlated ($r = 0.00$). The results of the fitting are robust with respect to changes in the periods of the analyses and are not noticeably affected by the detrending.

Figures 4 and 5 show the effects of removing the T_{ENSO} and T_{dyn} time series from all three global-mean time series. The T_{dyn} time series evidently accounts for a component of the month-to-month variability in T_g and T_{Land} (Figs. 4 and 5b), whereas T_{ENSO} accounts for much of the interannual variability in all three time series (Figs. 4, 5a, and 5b). The T_{ENSO} and T_{dyn} residual time series (bottom

time series in all panels) provide a comparatively smooth rendition of the global-mean temperature variability, and they also serve to highlight a number of sudden drops in surface temperatures over the past century. The drop in late 1945, which is largely restricted to the T_g and T_{SST} time series, is attributable to changes in SST measurement methods, as discussed in Thompson et al. (2008). Many of the other major drops are coincident with large tropical volcanic eruptions (indicated by the dashed vertical lines) and are considered in the following section.

4. The volcanic signal in the T_{ENSO} and T_{dyn} residual data

In this section we document the volcanic signal in the data formed by subtracting from global-mean temperatures the effects of ENSO and dynamically induced variability. In section 5 we will outline a methodology for removing the signal of volcanic eruptions from global-mean surface temperature time series.

Large volcanic eruptions impact climate primarily via the injection of sulfur-rich volatiles into the atmosphere

a) Global-mean ocean temperatures
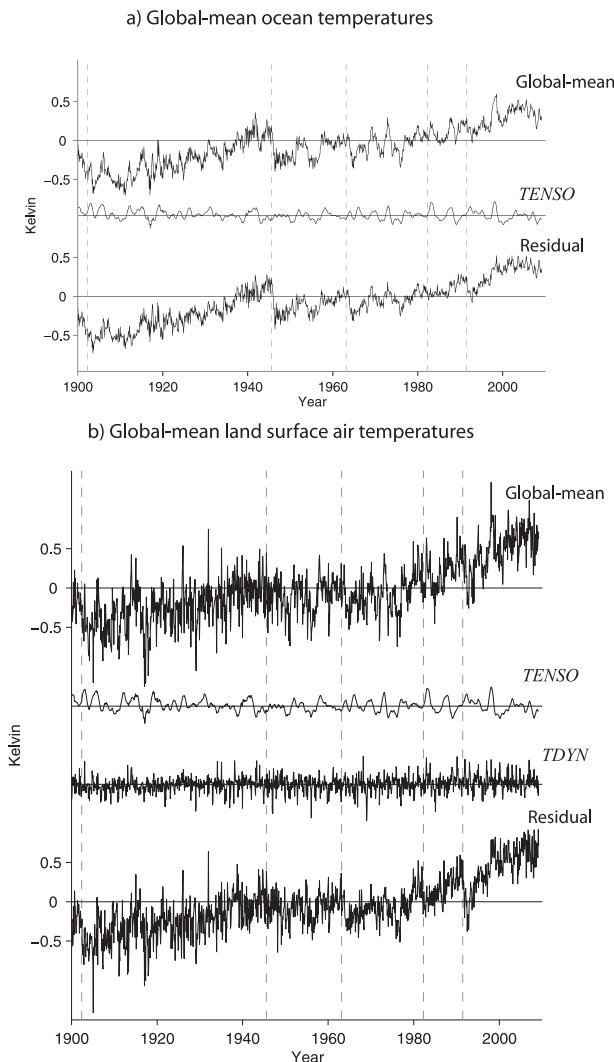
b) Global-mean land surface air temperatures

FIG. 5. As in Fig. 4, but for (a) global-mean SSTs from the HadSST2 dataset and (b) the global-mean surface land data from the CRUTEM3 dataset. Note that T_{dyn} is not significantly correlated with the global-mean SST time series and hence is not filtered from the SST data.

[see the review by Robock (2000) and references therein]. Within a few months of the eruption, the volatiles condense to form sulfuric-acid aerosols, and the resulting aerosol cloud scatters shortwave radiation while absorbing longwave radiation. The scattering of shortwave radiation acts to cool the surface whereas the absorption of longwave radiation acts to warm the stratosphere (e.g., Stenchikov et al. 1998). In the case of large tropical eruptions, the meridional gradients in stratospheric heating give rise to anomalously westerly flow at middle latitudes not only in the lower stratosphere, but also at the earth's surface (Robock and Mao 1992; see also the discussion in Robock 2000).

The impacts of volcanic eruptions on global climate depend primarily on 1) the amounts of volatiles that reach stratospheric levels and 2) the latitudes of the eruptions. Volatiles that remain in the troposphere are scavenged within a few months of the eruption and thus do not have a long-lasting impact on global climate; volatiles ejected by high-latitude eruptions are restricted primarily to the eruption hemisphere by the predominantly poleward meridional Brewer–Dobson circulation in the middle-latitude stratosphere. On the basis of such criteria, previous studies have identified the most climatically important volcanic events of the twentieth century to be the eruptions of Mounts Pelée–Soufrière–Santa Maria (in Martinique, St. Vincent, and Guatemala, respectively) between May and October 1902, Mount Agung (on the Indonesian island of Bali) in March 1963; El Chichón in April 1982 (in Mexico); and Mount Pinatubo in June 1991 (on the island of Luzon in the Philippines) (Robock 2000).

The surface cooling following the largest eruptions of the twentieth century has been widely documented (e.g., see Jones et al. 2003 and references therein). However, the amplitude and time scale of the cooling associated with individual eruptions is difficult to ascertain for two reasons: 1) the eruptions are superimposed upon temperature variations due to nonvolcanic causes and 2) over the NH continents, the radiatively driven cooling is opposed by the dynamically induced warming associated with volcanic eruptions (Robock and Mao 1992). Previous studies have examined the volcanic signal in data adjusted for the effects of ENSO and trends in surface temperatures (e.g., Mass and Portman 1989; Santer et al. 2001). But to our knowledge, no previous study has examined the signal of volcanic cooling in temperature data after accounting for the effects of dynamically induced variability.

The obfuscation of the volcanic cooling by dynamically induced variability is exemplified in the response of global-mean temperatures to the June 1991 eruption of Mount Pinatubo. The left and middle panels in Fig. 6 are excerpts from the combined land and ocean global-mean temperature time series (T_g) and residual T_g time series from Fig. 4 but focused on the period surrounding the June 1991 eruption of Mount Pinatubo. The right panel in Fig. 6 shows the residual T_g time series after the 30-yr trend centered on the June 1991 eruption date has been removed from the data. The cooling following the eruption of Mount Pinatubo is barely discernible in T_g (Fig. 6, left) because it is masked by ENSO-related and dynamically induced variability in the record. The volcanic signal is evidently much clearer in the residual global-mean time series (Fig. 6, middle) but is distorted by the pronounced global warming trend of the past few decades. The volcanic signal is most clearly isolated when the low-frequency global-scale warming of the
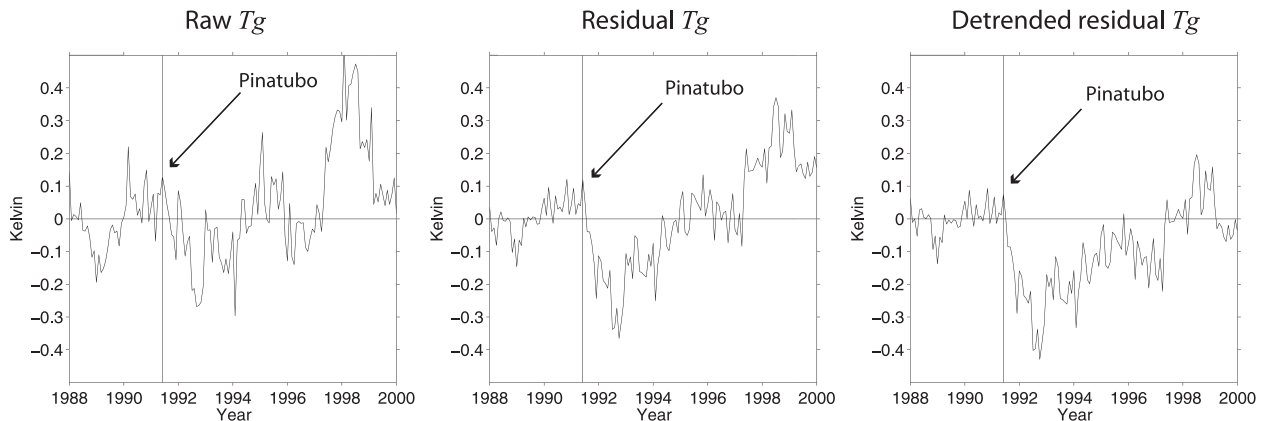
FIG. 6. (left and middle) The global-mean and residual time series from Fig. 4 but focused on the period surrounding the June 1991 eruption of Mount Pinatubo. (right) As in the middle panel but the 30-yr trend centered on the eruption date has been removed from the data. The vertical lines denote the June 1991 eruption date; the horizontal lines denote the mean for the 4-yr period preceding the eruption date.

past decades has been removed from the residual time series (Fig. 6, right). The results in the right panel in Fig. 6 suggest global-mean temperatures dropped by nearly 0.4 K after the eruption of Mount Pinatubo, an amplitude that is comparable to the independently derived estimate found in Santer et al. (2001).

The refinement of the Mount Pinatubo eruption signal in Fig. 6 is also evidenced in association with the other large volcanic eruptions of the twentieth century. Figure 7 shows temperatures averaged across the four largest eruptions of the twentieth century for raw time series (left column), residual time series (middle column), and detrended residual time series (right column; results for individual eruptions are presented in appendix A). The top panels in Fig. 7 show the results for T_g, the middle panels for T_{Land}, and the bottom panels for T_{SST}. The composites are shown with respect to the climatology for the 4-yr period prior to the eruptions, and are referenced with respect to the first January following the eruptions to account for the phase locking of the volcanic signal with the annual cycle (e.g., Robock and Mao 1992). As in Fig. 6, the results in the right column of Fig. 7 are detrended by removing the 30-yr trend centered on the eruption dates. Tick marks are shown for Januarys, and the first January following the eruptions is denoted as lag 1. The 95% confidence levels (horizontal dashed lines) are calculated separately for each time series and denote values that are exceeded only 5% of the time in 10^4 randomized sortings of the composite dates.

The composites in the left column in Fig. 7 are reminiscent of similar analyses shown in previous studies (see Jones et al. 2003 and references therein). The results reveal significant global-mean cooling following the eruption date, but the cooling spans only ~2 yr and is

matched by similarly large values ~6 yr prior to the eruption date. The cooling over the land areas is slightly larger than that over the ocean areas, but the temperature response over land is noisy and only weakly significant. The warming of the NH continents during the first winter following the eruptions is apparent as weak warming at lag 1 in the T_{Land} composite [Fig. 7, middle panel of left column; see also Robock and Mao (1992)], but this feature is not significant in the global mean.

The composites based on the data filtered for the effects of ENSO and dynamically induced variability (Fig. 7, middle column) give a clearer representation of the radiatively driven surface cooling associated with volcanic eruptions. The noise in the composite results is greatly reduced, and the cooling following the eruption date is both smoother and more statistically significant. The emergence of the radiatively driven volcanic cooling is particularly pronounced over land where the filtering methodology accounts for not only random dynamically induced variability but also the warming of the continents due to the dynamical impact of volcanic eruptions. As in Fig. 6, the eruptions stand out even more clearly when the 30-yr trends centered on the eruption dates are removed from the data (Fig. 7, right column).

The results in the right column of Fig. 7 provide the cleanest rendition of the radiative cooling due to volcanic eruptions that we are aware of in the existing literature based on the instrumental record. They are similar in some respects to a composite of 50 volcanic eruptions between 1400 and 1940 presented by Hegerl et al. (2003) in which the timing of the eruptions is inferred from records of ice-core aerosol optical depth and year-to-year variations in Northern Hemisphere temperature are inferred from tree-ring reconstructions. The results presented in this study and Hegerl et al.
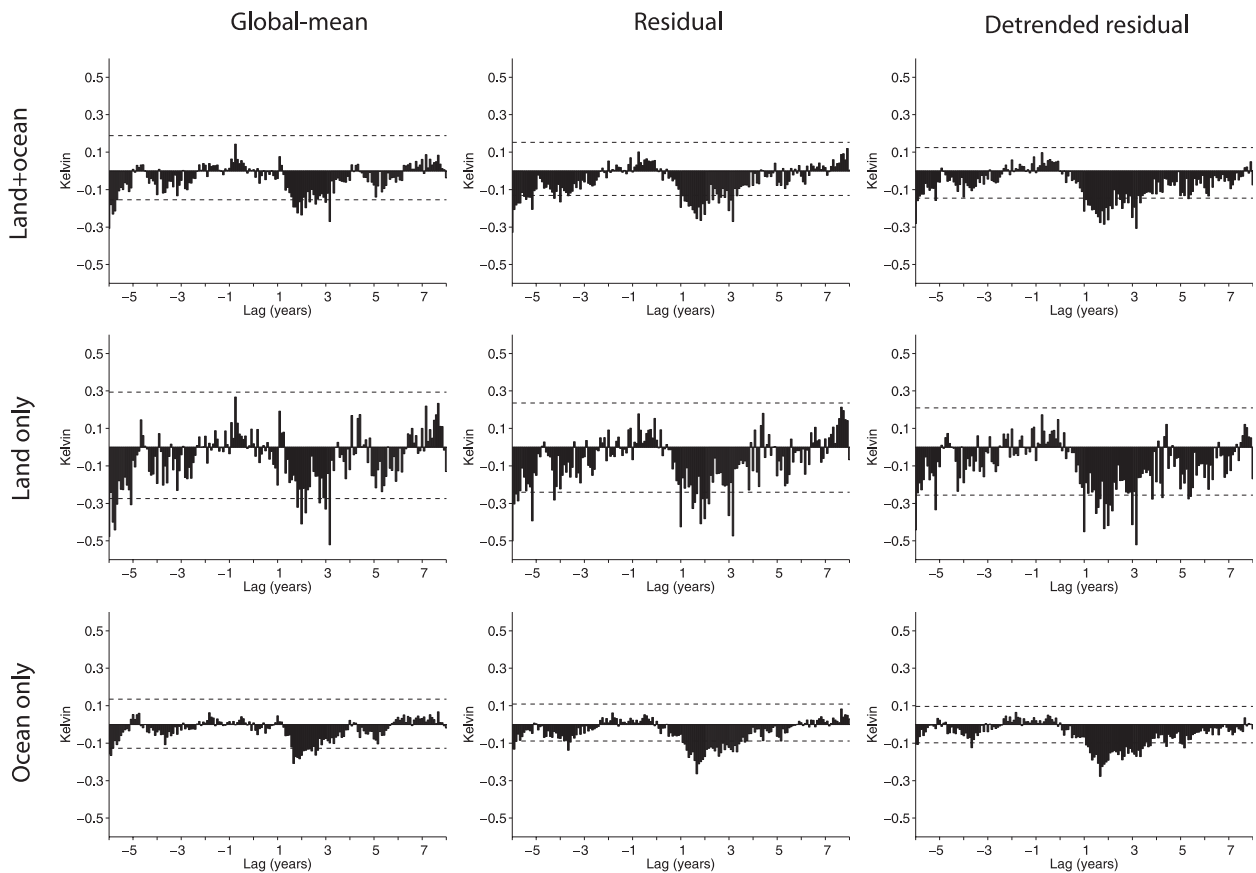
FIG. 7. Composite response to the eruptions of Santa María, Mount Agung, El Chichón, and Mount Pinatubo. (left) results calculated for raw (i.e., unfiltered) global-mean surface temperature data from Figs. 4 and 5. (middle) Results calculated for the T_{ENSO} and T_{dyn} residual global-mean data from Figs. 4 and 5. (right) As in the middle column but for data detrended for the 30-yr period centered on the eruption dates. Results are averaged as a function of calendar month and values of zero denote the mean for the 4 yr before the eruption date. Lag 1 denotes the first January after the eruption date. Horizontal lines denote the 5% and 95% confidence levels for individual months with respect to the mean for the 4 yr before the eruption date.

(2003) both suggest that the recovery time scale is on the order of 7 yr: considerably longer than the ~2–3 yr suggested in the composites in the left panel of Fig. 7. The ~7 yr recovery time is evident not only over the oceans but over land areas as well (Fig. 7, right column).

In the following section, we provide a methodology for removing the volcanic signal from the global-mean temperature data, and demonstrate that the ~7 yr time scale is physically consistent with the damped thermodynamic response of the oceanic mixed layer to comparatively short-lived volcanic radiative forcing.

5. Removing the volcanic signal from global-mean temperatures

The methodology used to remove the volcanic signal from global-mean temperatures is analogous to that used in section 3 to remove ENSO. In the case of ENSO, we drove the Hasselman climate model with the time series of estimated anomalous heat fluxes in the eastern tropical Pacific; in the case of volcanic eruptions, we drive the same equation with the time series of estimated volcanic radiative forcing. The response of the global ocean–atmosphere system to volcanic forcing is thus modeled as

$$C \frac{d}{dt} T_{\mathrm{Volcano}}(t) = F(t) - \frac{T_{\mathrm{Volcano}}(t)}{\beta}, \qquad (5)$$

where T_{Volcano} denotes the simulated response of monthly mean global-mean surface temperature anomalies to the forcing associated with volcanic eruptions, $F(t)$ is the global-mean volcanic radiative forcing, β is the climate sensitivity used in Eq. (1), and C is the heat capacity of the global atmospheric–oceanic mixed layer per unit area.

The global-mean volcanic forcing is shown as the top time series of Fig. 8. The forcing is derived from optical
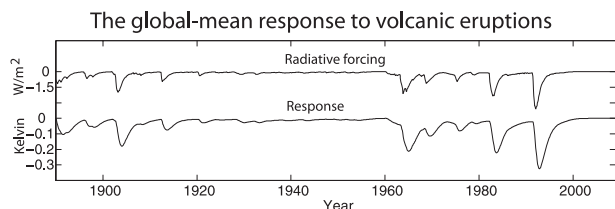
FIG. 8. (top) Volcanic radiative forcing based on updated data described in Sato et al. (1993) and obtained from NASA GISS. (bottom) The response of global-mean temperatures to the radiative forcing in the top curve, as estimated by Eq. (5).
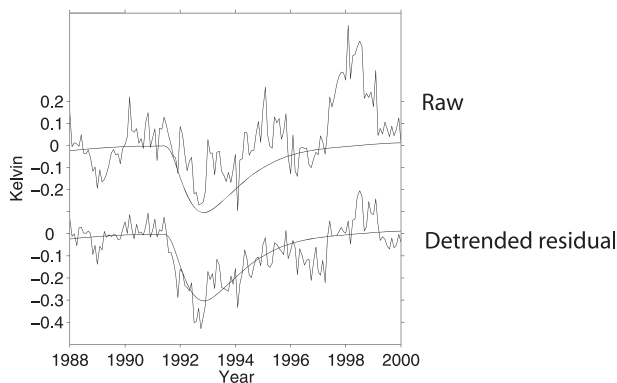

FIG. 9. The jagged black lines show the (top) raw and (bottom) detrended residual global-mean temperature time series reproduced from Fig. 6. The smooth curves show the response to volcanic radiative forcing reproduced from Fig. 8.

depth measurements given by Sato et al. (1993), and the optical depth data are multiplied by a factor of 24 W m^{-2} per unit optical depth to convert them to an equivalent radiative forcing (Hansen et al. 2005). The volcanic forcing data were obtained from the National Aeronautics and Space Administration's Goddard Institute for Space Studies (NASA GISS). The estimated forcing is most reliable over the past few decades when satellite measurements are widely available, but the general characteristics of the forcing are broadly reproducible over the last half of the twentieth century in other major reconstructions (e.g., Ammann et al. 2003). The global-mean forcing peaks at around -3 W m^{-2} during the period immediately following the eruption of Mount Pinatubo.

As was done for ENSO, the effective heat capacity in Eq. (5) is determined empirically so that the correlation coefficient is maximized between detrended values of $T_{Volcano}$ and T_g. In the case of volcanic eruptions the correlation is maximized for the period surrounding the eruption of Mount Pinatubo (1988–2000) since 1) the forcing is well known for this eruption and 2) the period immediately following the eruption is not complicated by the superposition of a large ENSO event, as is the case for the eruption of El Chichón. The resulting effective heat capacity ($C \sim 4.8 \times 10^7$ J m^{-2} K^{-1}) is equivalent to the global atmosphere plus $\sim$9 m of the global oceanic mixed layer. Note that the larger heat capacity used to drive Eq. (5) relative to Eq. (1) is consistent with the longer time scale of the forcing associated with volcanic eruptions than with individual ENSO events. The $T_{Volcano}$ time series was fit to the three residual global-mean time series in Figs. 4 and 5 using the regression methodology outlined in Eq. (4).

The global-mean fit to $T_{Volcano}$ is shown as the bottom time series in Fig. 8. Both the forcing and the global-mean temperature response are dominated by the eruptions of Mounts Pelée–Soufrière–Santa Maria (between May and October 1902), Mount Agung (March 1963), El Chichón (April 1982), and Mount Pinatubo

(June 1991). But the Sato et al. (1993) time series also reflects lesser loadings due to the smaller eruptions of, for example, Mount Katmai (1912) in Alaska, Fernandina Island (1968) in the Galápagos Islands of Ecuador, and Mount Fuego (1974) in Guatemala. As is the case for ENSO, the thermodynamic model acts to low-pass filter and lag the input forcing time series.

The quality of the fit between the observed global-mean temperatures and $T_{Volcano}$ is exemplified by Fig. 9. The jagged lines in the top and bottom curves are reproductions of the global-mean and detrended residual global-mean time series from the left and right panels of Fig. 6, respectively; the smooth curves show the estimate of the response provided by $T_{Volcano}$. As noted in section 4, the eruption of Mount Pinatubo is difficult to discern in the raw data (Fig. 9, top) but is readily apparent in the ENSO and T_{dyn} residual time series (Fig. 9, bottom). As is evident in Fig. 9, the $T_{Volcano}$ time series provides an excellent fit to the refined volcanic signal provided by the residual data.

Figure 10 shows the eruption residual time series obtained by subtracting $T_{Volcano}$ from the three global-mean temperature time series considered in this study: T_g, T_{Land}, and T_{Ocean}. The methodology evidently accounts for virtually all of the decreases in the global-mean temperatures following the eruptions of El Chichón and Mount Pinatubo, but not all of the decreases in temperatures following the 1902 eruptions of Mounts Pelée–Soufrière–Santa Maria and the 1963 eruption of Mount Agung. The shortcomings of the fit in 1902 are not surprising since both the temperature data and the forcing are less reliable for that time. As noted in the following section, the apparent signal of Mount Agung in the eruption residual data may reflect changes in SST instrumentation or an underestimate of the forcing
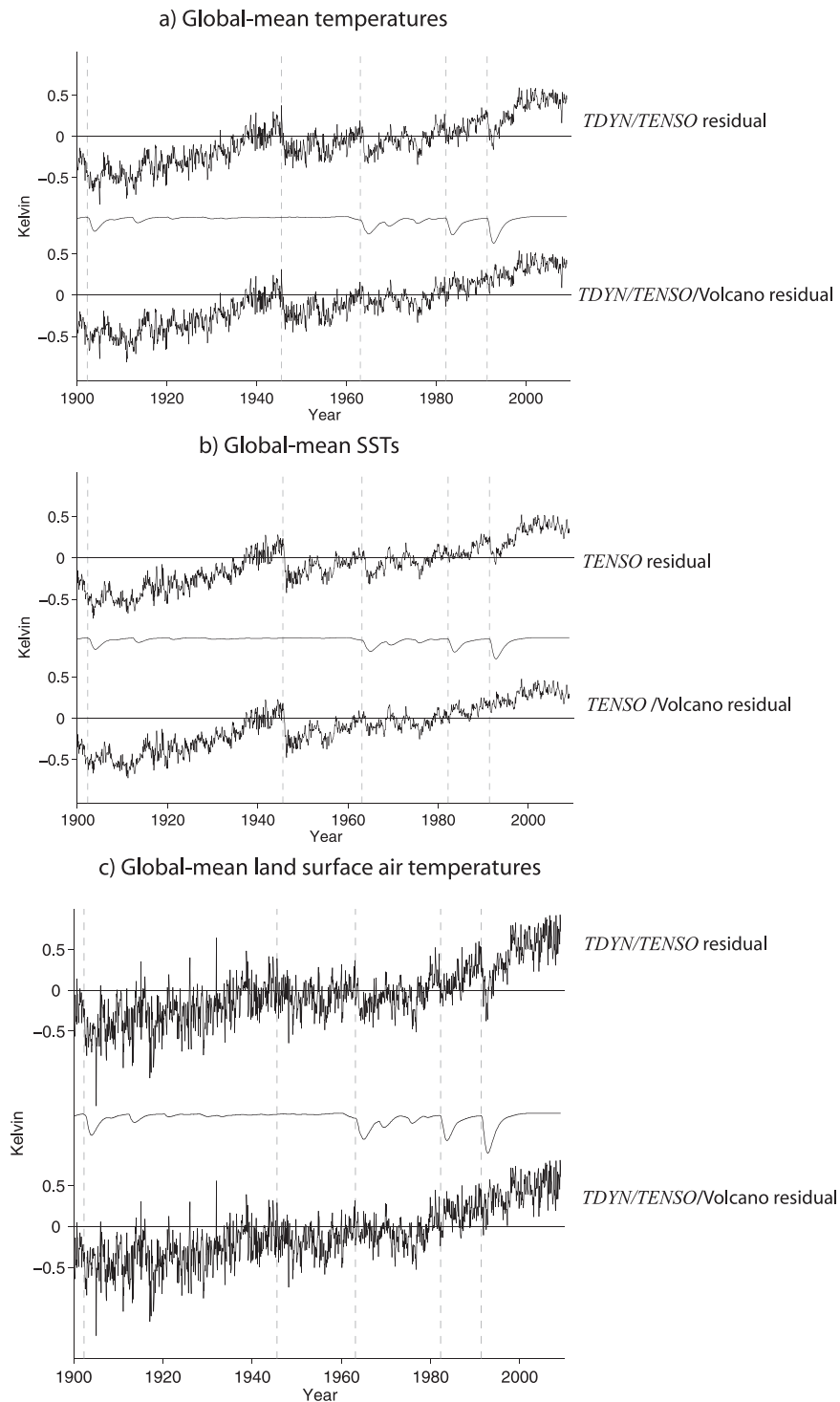
a) Global-mean temperatures

b) Global-mean SSTs

c) Global-mean land surface air temperatures

FIG. 10. Subtracting the volcanic signal from the T_{dyn} and T_{ENSO} residual global-mean data. In all panels, the top time series is a reproduction of the appropriate T_{dyn} and T_{ENSO} residual time series from Figs. 4 and 5, the middle series is the volcanic fit, and the bottom is the resulting T_{dyn}, T_{ENSO}, and volcanic residual time series. (a) The results for the combined global-mean land and SST time series. (b) The results for global-mean SST data. (c) The results for global-mean land temperature data. Note that T_{dyn} is not filtered from the SST time series (see Fig. 5 caption and text).
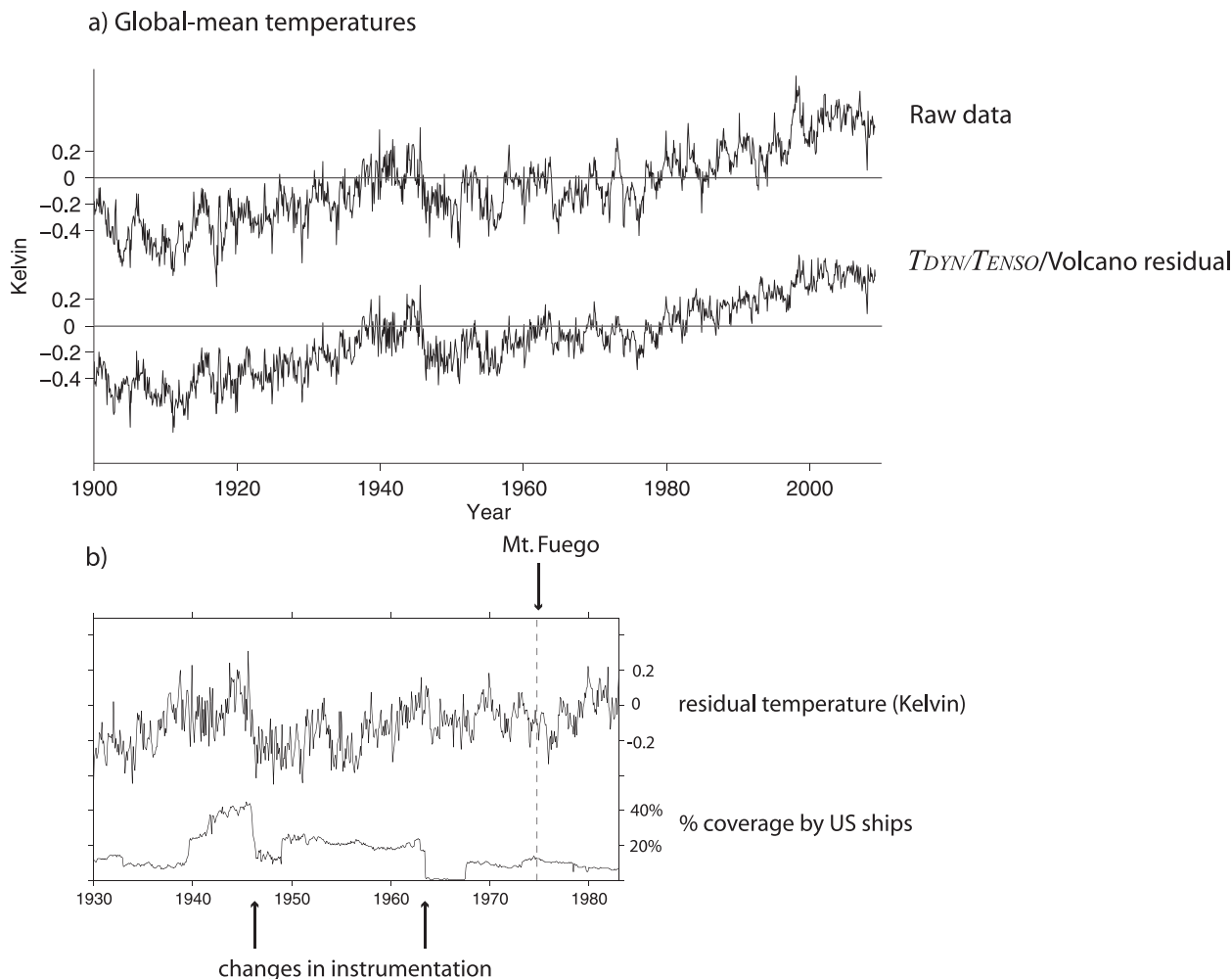
FIG. 11. (a, top series) The raw (unfiltered) combined land and ocean global-mean temperature time series (reproduced from Fig. 4). (a, bottom series) The residual global-mean temperature time series formed by regressing T_{dyn}, T_{ENSO}, and the volcanic signal from the global-mean data (reproduced from Fig. 10). (b) The residual temperature time series reproduced from the top panel alongside the percentage of SST observations derived from U.S. ships.

associated with the eruption. The implications of the volcanic eruption residual time series for the interpretation of twentieth-century climate variability are discussed in the following section.

6. Discussion and implications

The results of the filtering methodology provide a remarkably clean rendition of twentieth-century global-mean temperature variability. When the ENSO and dynamically induced variability are removed from the global-mean temperature time series, the analyses highlight the spurious drop in SSTs in 1945 and draw out the signal of major volcanic eruptions in surface temperatures (Figs. 4 and 5). When the signal of volcanic eruptions is subsequently removed from the data, the

time series are dominated by century-long warming that is punctuated primarily by 1) the step in global-mean temperatures in ~1945 and 2) a brief cooling in the 1970s (Fig. 10). In this section we discuss three aspects of twentieth-century temperature variability highlighted by the residual data: the long-term trends, the coupling between the ocean and land time series on the interannual time scale, and a change in the properties of the land time series around 1945–50.

a. Long-term trends

Figure 11a summarizes the implications of the methodology outlined here for the interpretation of long-term trends in global-mean temperature. The top panel in Fig. 11 shows the raw and residual time series of global-mean temperature T_g repeated from Figs. 4 and

10a, respectively, where the residual time series is fil-
tered for the effects of ENSO, dynamically induced
variability, and volcanic eruptions. The residual time
series is dominated by variability on very long time
scales, namely the rise in temperatures during the first
half of the century, the sudden drop in global-mean
temperatures in late 1945, and the nearly monotonic rise
since ~1950. The drop in 1945 is consistent with changes
in SST measurement techniques as recorded in the ar-
chive of SST measurements (Thompson et al. 2008). But
a concurrent—albeit much weaker and shorter lived—
dip is also apparent in the residual land time series (Fig.
10c). The nearly monotonic warming from ~1900 to
1945 and from ~1950 to the current day is reflected in
both the residual land and ocean time series in Figs. 10b
and 10c.

The nearly monotonic warming in the residual time
series since ~1950 is punctuated most notably by 1) a
drop in temperatures in ~1963, 2) brief cooling in the
middle 1970s, and 3) a flattening since the late 1990s.
The drop in 1963 coincides with a decrease in the
number of SST measurements derived from U.S. ships
(Fig. 11b). As discussed in Thompson et al. (2008), U.S.
SST measurements were biased warm relative to SST
measurements from the United Kingdom in the middle
twentieth century, and might have been biased warm
relative to SST measurements from other countries in
the 1960s. Hence, the drop in 1963 may reflect changes
in the mix of SST measurements. However, the drop in
1963 also coincides with the eruption of Mount Agung
and is weakly apparent in the residual global-mean land
time series (Fig. 10c). Hence, it is also plausible that the
drop in 1963 reflects an underestimate of the amplitude
of the eruption by the Sato et al. (1993) volcanic forcing
used here. The slight decline in the residual time series
from 1970 to about 1977 is not coincident with known
changes in measurement techniques, nor is it clearly
tied to the only large eruption that occurred during the
1970s (Mount Fuego; Fig. 11b). As shown later, the
flattening of global-mean temperatures since the late
1990s is derived primarily from the SST data. To what
extent the flattening is affected by recent changes in SST
measurements is currently under investigation (Worley
et al. 2005; Rayner et al. 2006; Forest and Reynolds
2008).

b. Coupled ocean–land temperature fluctuations

The residual data also highlight the existence of
temperature variations on the interannual time scale
that exhibit a high degree of coupling between the land
and ocean areas that is not attributable to ENSO and
volcanic eruptions. The top time series in Fig. 12 are
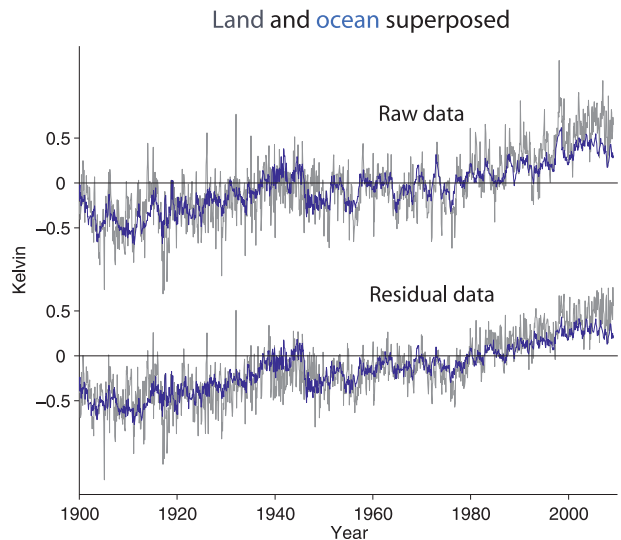superposed values of the raw global-mean land and SST

FIG. 12. The (top) raw and (bottom) residual land and SST time
series (gray and blue, respectively). The raw time series are re-
produced from Fig. 5; the residual time series are reproduced from
Fig. 10. The correlations for the period January 1950–December
2006 are $r = 0.84$ ($r = 0.63$ after detrending the data) for the top
time series and $r = 0.85$ ($r = 0.49$ after detrending the data) for the
bottom time series.

time series transcribed from Figs. 5a and 5b; the bottom
pair are the corresponding superposed values of the
T_{ENSO}/T_{dyn}/volcano residual time series transcribed
from Figs. 10b and 10c. The raw time series are highly
correlated, in large part because ENSO and volcanic
eruptions affect both land and ocean temperatures
(Fig. 12, top). But surprisingly, the residual time series
are also strongly correlated, even after detrending. The
residual land and ocean time series in Fig. 12 track each
other remarkably well throughout much of the twentieth
century with two notable exceptions: the large drop in
SSTs in 1945 and the amplified warming of the land
areas since ~1980. The correlations between detrended
values of the global-mean land and SST time series
calculated for the period 1950–2006 are $r = 0.63$ for the
raw data and $r = 0.49$ for the residual data (both exceed
the one-tailed 99% confidence level).

Figure 13 illustrates the coupling between the raw and
residual global-mean time series in Fig. 12 in more de-
tail. The curves labeled "all timescales" in the top panels
of Fig. 13 represent lag correlations between detrended
values of the global-mean land and SST time series for
the raw (left) and residual (right) data. Negative lags
denote the land time series leading SSTs, and vice versa.
For both the raw and residual data, the correlations peak
near lag 0 but are not symmetric about their maximum
values. At a given lag they are larger when the SST field
leads. The amplitudes of the correlations are larger for

a) Lag correlations between the detrended raw land and ocean time series

c) Lag correlations between the detrended residual land and ocean time series

b) raw land and ocean time series (interannual timescales)

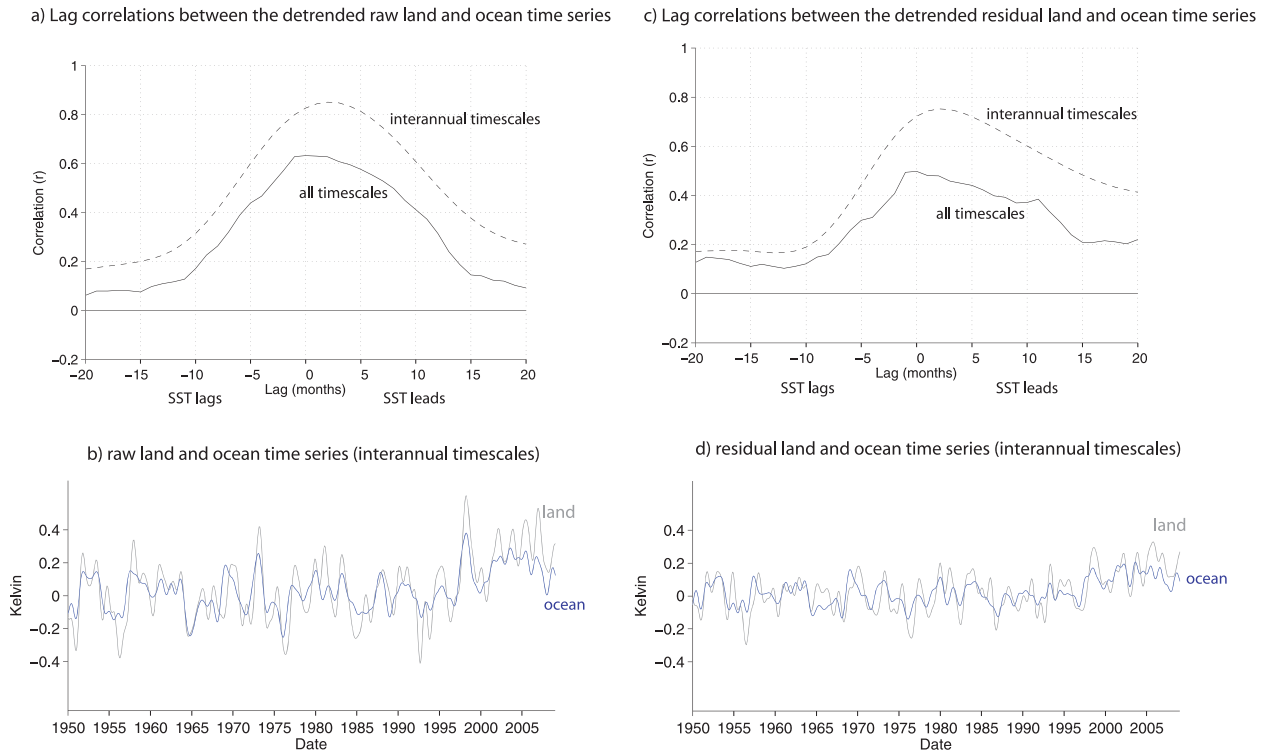d) residual land and ocean time series (interannual timescales)

FIG. 13. (a) Lag correlations between detrended values of the raw (i.e., unfiltered) land surface temperature and SST time series from Fig. 12. Results are shown for interannual and all time scales (where interannual is defined as 1–20-yr bandpass filtered). (b) The interannual versions of the raw land surface temperature and SST time series. (c),(d) As in (a),(b), but for analyses based on the residual land and SST time series from Fig. 12.

the raw data, but the asymmetry of the correlations about lag 0 is more striking for the residual data.

The asymmetry in the correlations is accentuated in lag correlations calculated for 1–20-yr (i.e., 12–240 month) bandpass-filtered versions of the time series (labeled "interannual" in the top panels in Fig. 13). Similar results are obtained for high cutoff frequencies of 6, 12, and 24 months (not shown). For both the raw and residual data, the correlations based on interannual data have substantially higher amplitudes and peak when the SST time series leads by ~2–3 months. However, the asymmetry in the lag correlations is more pronounced in the residual data. Both the significant covariability and the ~2–3 month lag between the ocean and land time series are visually apparent in the interannual versions of the time series (Fig. 13, bottom panels).

As noted earlier, covariability between the raw global-mean land and SST time series is to be expected since ENSO projects onto both land and ocean areas. But the coupling between the residual time series is surprising since ENSO has been linearly removed from both the land and SST time series. The observed coupling documented in Fig. 13 provides observational support for analogous coupling found in climate simu-

lations forced by prescribed SST anomalies (e.g., Zhang et al. 2007; Compo and Sardeshmukh 2008; Hoerling et al. 2008; Dommenget 2009).

Is the observed covariability between the residual global-mean land and SST time series derived from any particular region of the globe? Figure 14 shows the correlation map formed by regressing gridded SST data onto the residual interannual global-mean land time series (i.e., the gray time series in Fig. 13, bottom right; note that ENSO, volcanic eruptions, and dynamically induced variability are removed from the global-mean land time series but not from the gridded SST data since the filtering methodology is only applicable to area averages). The correlation map reveals scattered areas of positive correlations over all three oceans, but in general the correlations are most coherent over the tropical and northern North Atlantic; that is, much of the covariance between the residual land and ocean time series in Figs. 12 and 13 is derived from SST variability in the Atlantic Ocean north of the equator. The correlations between 1–20-yr bandpass-filtered SST anomalies averaged over the North Atlantic Ocean poleward of the equator and the global-mean residual land time series are statistically significant but are largest at zero lag ($r = 0.39$; exceeds

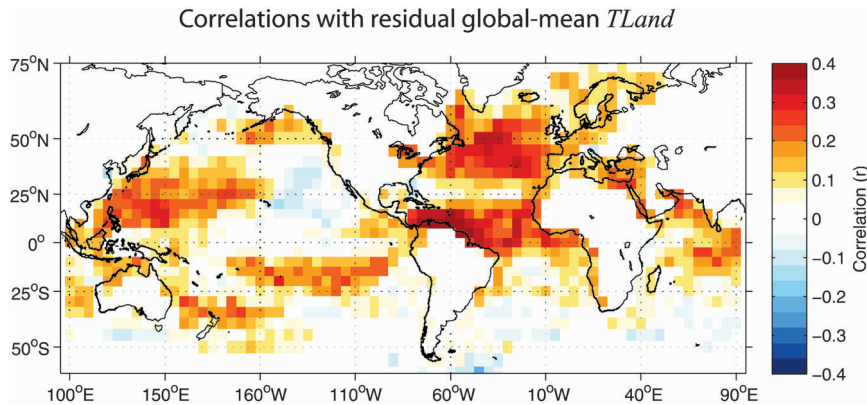Correlations with residual global-mean *TLand*

FIG. 14. Correlations between the raw (i.e., unfiltered) SST data and the residual global-mean land temperature time series. The residual land time series is the T_{dyn}/T_{ENSO}/volcanic residual time series, and is filtered to retain only interannual variability between 1 and 20 yr (i.e., it is the land time series from the bottom right of Fig. 13).

the 97.5% significance level), not when the SST field leads (results not shown).

c. The drop in high-frequency variance in global-mean land temperature data in the 1940s

Another aspect of global-mean temperature variability highlighted by the filtering technique is the change in the mean value and month-to-month variability of the residual land temperature time series around ~1945–50. The timing of the apparent change in the statistical properties of the land data is of particular interest since it coincides with the sudden drop in SSTs. The top time series in Fig. 15 shows the residual land time series transcribed from Fig. 10c. The decrease in variance ~1945–50 is visually apparent in the residual global-mean time series but is objectively verified by plotting the derivative and the absolute value of the derivative of the time series (Fig. 15, second and third time series from the top). Taking the time derivative amplifies the high-frequency sampling variability in the record, much of which is attributable to the incomplete spatial coverage of the station network, and taking the absolute value of the derivative reveals its evolution more clearly. The outstanding features are the decline in sampling variability during the late 1940s and the weaker increase after ~1990.

The curve at the bottom of Fig. 15 shows the fraction of the globe covered by the gridded land data (defined as the cosine-weighted global percentage of grid boxes with at least one reporting station). The drop in variance in the land time series in the late 1940s is broadly consistent with the time history of the coverage of the land surface temperature observing network. We test this

hypothesis by showing the same temperature time series in Fig. 16, but calculated only from grid boxes with at least 50% coverage between 1900 and 1940. Freezing the spatial coverage to the pre-1940 era eliminates most, albeit not all, of the decrease in the sampling variability during the mid–twentieth century.

7. Concluding remarks

The purpose of this paper is to develop and apply a robust, simple, and physically based methodology for the removal from global-mean temperatures of the
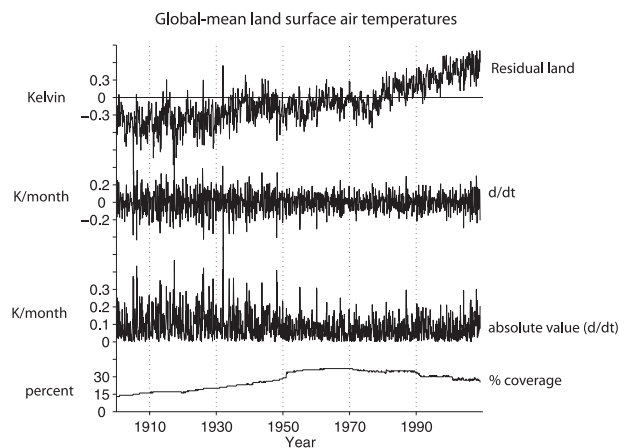

FIG. 15. (top) The residual global-mean surface land temperature time series from Fig. 10. (second from top) The time derivative of the top time series. (second from bottom) The absolute value of the time derivative. (bottom) Time history of the percentage of station coverage used in the CRUTEM3 data (defined as the cosine-weighted global percentage of grid boxes with at least one reporting station).
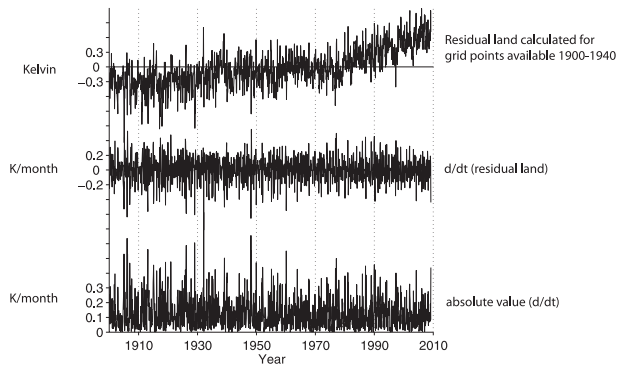
FIG. 16. As in the top three time series in Fig. 15, but for the residual global-mean land surface temperature time series calculated for grid points with at least 50% coverage between 1900 and 1940.

variability associated with known climate phenomena. Previous studies have estimated the signals of ENSO, volcanic eruptions, and internal atmospheric variability in global-mean temperatures using various regression methodologies. But as far as we know, this is the first study to 1) represent the signals of ENSO and volcanic eruptions using a simple thermodynamic model of the climate system, 2) use the SLP pattern most strongly coupled to the global-mean temperature time series to represent the effects of dynamically induced variability, and 3) explicitly remove (or filter out) the temporal signatures of these three sources of natural variability from global-mean temperature time series. The filtering methodology does not degrade the time resolution of the data. Hence, unlike filtering schemes based on temporal smoothing, this new approach yields a residual time series in which discrete changes in the time history of global-mean temperatures, including changes in instrumentation and explosive volcanic eruptions, are fully resolved.

The central findings highlighted by the filtering methodology include the following:

1) Filtering global-mean temperature time series to remove the effects of known sources of natural variability enriches the signal of the anthropogenically induced warming over the past century (Fig. 11a). The trends in the raw and residual data for the period January 1950–March 2009 are comparable (~0.12 K decade^{-1}); but the standard deviation of the (detrended) residual data is only 2/3 as large as the standard deviation of the raw data (~0.10 versus ~0.15 K). The residual time series shows more clearly the enhanced warming of the land areas relative to the ocean areas over the past few decades (Fig. 12). To what extent the differences between

ocean and land warming reflect the cooling bias in SSTs due to the recent transition from ship- to buoy-derived SSTs remains to be determined (Worley et al. 2005; Rayner et al. 2006; Forest and Reynolds 2008).

2) The residual time series show more clearly the signal of volcanic eruptions in surface temperature. For example, the signal of the eruption of Mount Pinatubo is barely discernible in the raw global-mean temperature time series (Fig. 6, left), but is clearly visible in the data filtered for the effects of ENSO and dynamically induced variability (Fig. 6, middle and right). The refined volcanic signal, with its longer decay time scale, should be more suitable for estimating climate sensitivity from observations of the climate system response to volcanic forcing.

3) The analyses reveal the existence of observed coupling between global-mean land and ocean temperatures on the interannual time scale, even after the effects of ENSO and volcanic eruptions are filtered out of the temperature time series. The observed coupling is largest when the SST field leads by ~2–3 months (Fig. 13) and is most prominent in the sea surface temperature variability in the North Atlantic Ocean (Fig. 14).

4) The analyses highlight the spurious discontinuity in global-mean temperatures in late 1945 (Fig. 11), and they also reveal a marked decrease in variance in the land temperature time series during the late 1940s (Fig. 15). The discontinuity in 1945 is derived largely from the SST field and appears to be related to the difference in SST measurement techniques between U.S. and U.K. ships in combination with an abrupt transition in the mix of marine observations from predominantly U.S. ships during World War II (WWII) to predominantly U.K. ships in the postwar years (Thompson et al. 2008). The drop in variance in the land data is coincident with rapid increases in the size of the observing network from ~1951 onward. It is worth noting that the land data also exhibit a small drop in the mean ~1945, although this decline is much smaller than that found in the residual SST time series (Fig. 10). The SST data corrected for instrument changes in the mid–twentieth century are expected to become available in 2010, and it will be interesting to see how the corrections affect the time history of global-mean temperatures, particularly in the middle part of the century.

The thermodynamic model used to estimate the signal of ENSO and volcanic eruptions provides a framework for deriving a "transfer function" that yields the global-mean temperature response to a prescribed forcing based
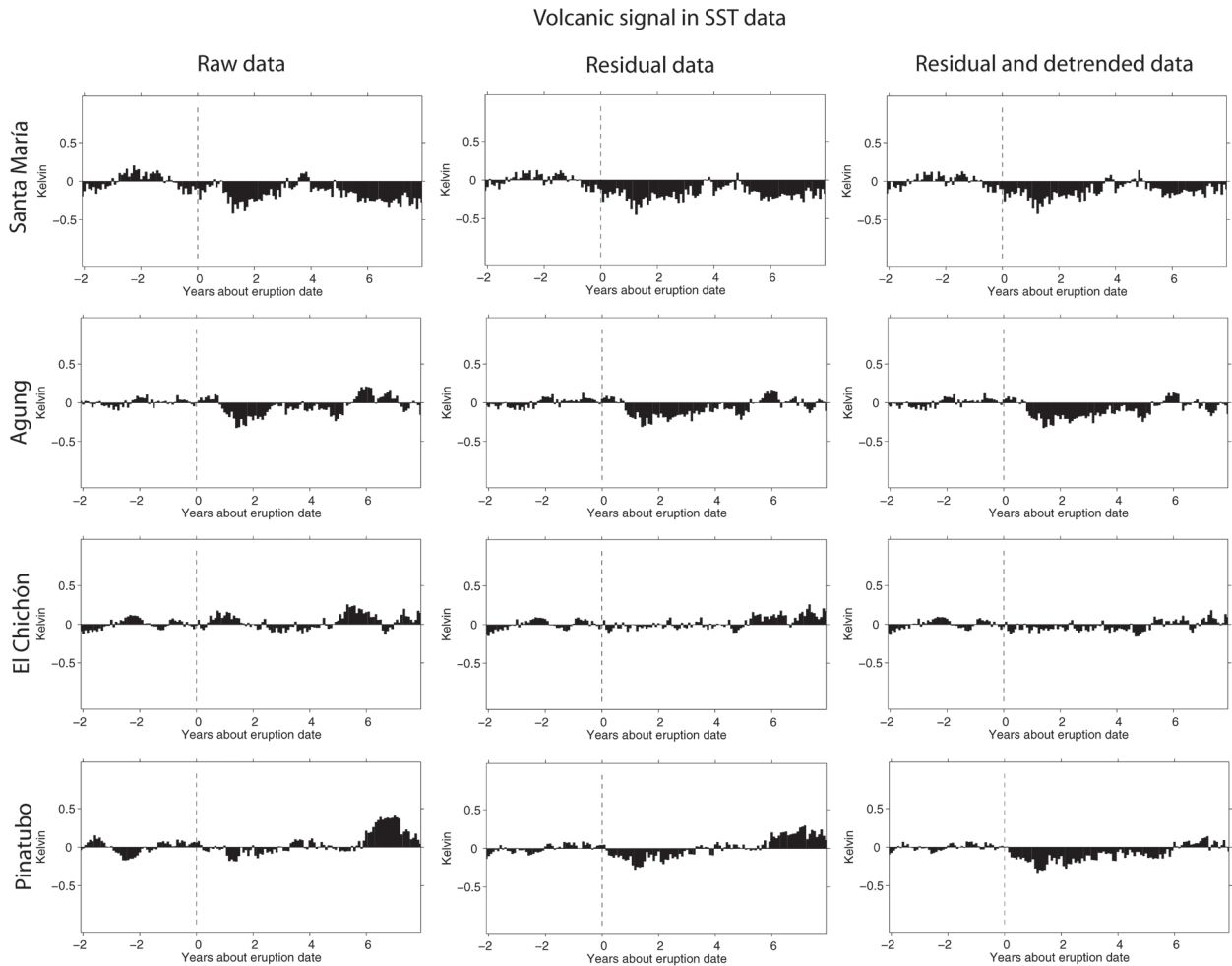
Volcanic signal in SST data

FIG. A1. As in Fig. 6, but for the raw, residual, and detrended residual SST time series focused on the period surrounding the four largest eruptions of the twentieth century. Year 1 denotes the first January after the eruption date.

on a simple least squares best fit. In addition to the fitted time series, the procedure yields an effective heat capacity, that is, the value of C that corresponds to the least squares best fit. Given a climate sensitivity of $\beta = 2/3$ K (W m^{-2})$^{-1}$, the effective heat capacity was found to be equivalent to the atmosphere plus a 2-m-deep ocean in the case of ENSO, and a 9-m-deep ocean in the case of volcanic eruptions. These estimates are only approximate in the sense that if they are doubled or halved, the fit between the observations and the model is degraded only slightly. Furthermore, the estimates do not imply that the signals of ENSO and volcanic eruptions are limited everywhere to the top 2 and 9 m of ocean, respectively; that is, the model is based on a globally averaged heat capacity and neglects the flux of heat into the deep ocean. In principle, the thermodynamic model can be used in a diagnostic manner to derive information about both the effective heat capacity and the climate

sensitivity, β. But we have not attempted to do that here because C and β are both dependent on the time scale of the forcing.

The filtering methodology should prove useful for investigating variations in global-mean temperature due to phenomena other than ENSO, variations in the high-latitude NH winter circulation, and volcanic eruptions (e.g., solar variability, variations in the oceanic thermohaline circulation, the effects of tropospheric aerosols, etc.). It could also be extended to include known sources of variability other than those considered here. For example, the pervasive negative correlations between surface temperature and precipitation over low-latitude regions, where local control of temperature via the evaporation from the underlying surface (Nicholls et al. 1996; Trenberth and Shea 2005) might be exploited to filter out additional variance of the temperature time series.
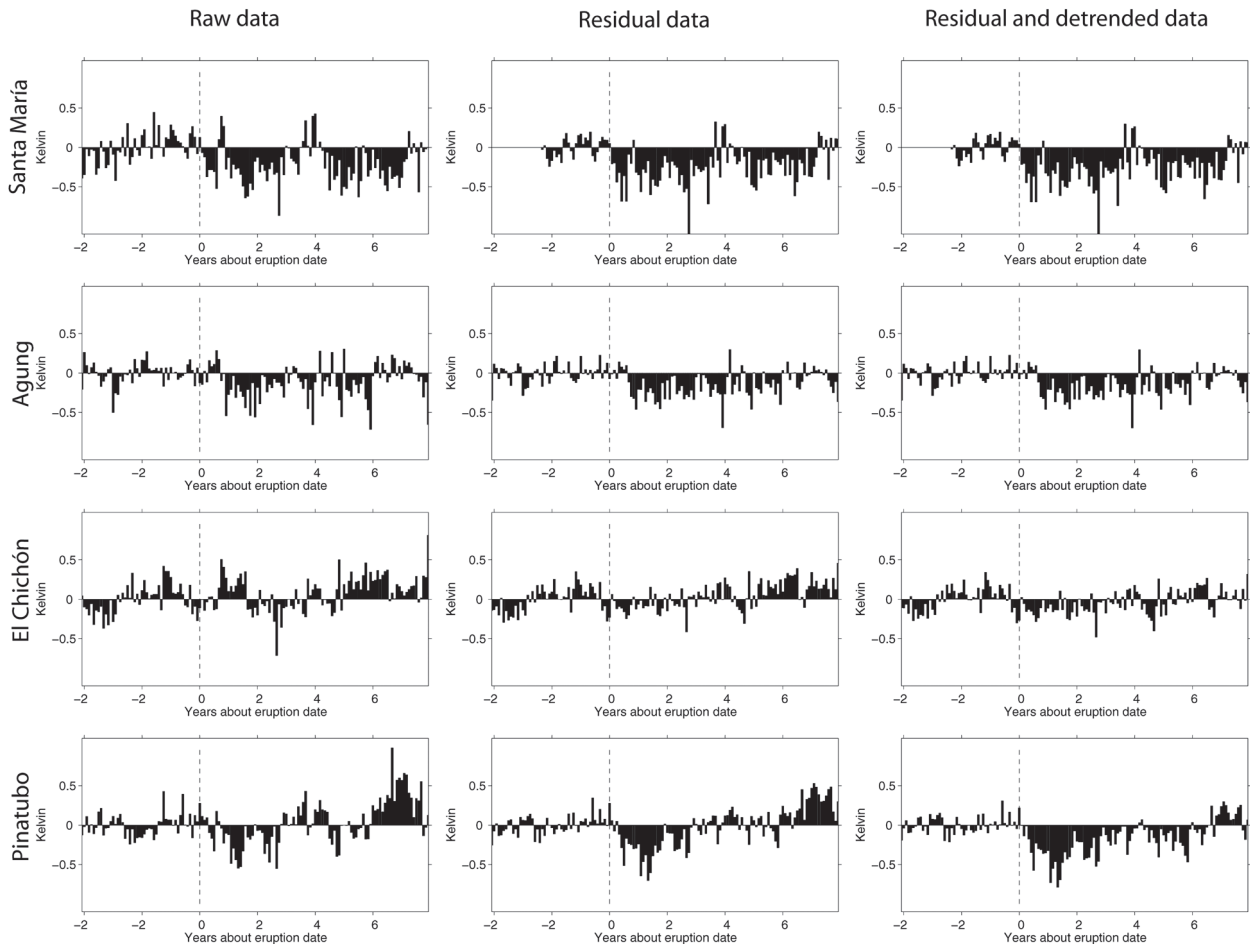
Volcanic signal in land data

FIG. A2. As in Fig. A1, but for the raw, residual, and detrended residual land surface temperature time series focused on the period surrounding the four largest eruptions of the twentieth century. Year 1 denotes the first January after the eruption date.

APPENDIX

Figures A1 and A2 document the volcanic signal in the global-mean SST and land data, respectively, for the four largest eruptions since 1900. The average of the results shown in Figs. A1 and A2 corresponds to the ocean and land composites in Fig. 7. As in Fig. 6, the left columns in Figs. A1 and A2 show the results for the raw data, the middle columns show the results for the residual data, and the the right columns the results for the detrended residual data. The data are detrended by removing the 30-yr linear trend centered on each eruption date. As was done for Fig. 6, the residual SST data are formed by removing the ENSO signal from the data; the residual land data are formed by removing the signatures of ENSO and dynamically induced variability from the data. Year 1 denotes the first January after each eruption.

REFERENCES

Ammann, C. M., G. A. Meehl, W. M. Washington, and C. S. Zender, 2003: A monthly and latitudinally varying volcanic forcing dataset in simulations of 20th century climate. *Geophys. Res. Lett.,* **30,** 1657, doi:10.1029/2003GL016875.

Barnett, T. P., M. Latif, E. Kirk, and E. Roeckner, 1991: On ENSO physics. *J. Climate,* **4,** 487–515.

Bretherton, C. S., M. Widmann, V. P. Dymnikov, J. M. Wallace, and I. Blade, 1999: The effective number of spatial degrees of freedom of a time-varying field. *J. Climate,* **12,** 1990–2009.

Broccoli, A. J., N.-C. Lau, and M. J. Nath, 1998: The cold ocean-warm land pattern: Model simulation and relevance to climate change detection. *J. Climate,* **11,** 2743–2763.

Brohan, P., J. J. Kennedy, I. Harris, S. F. B. Tett, and P. D. Jones, 2006: Uncertainty estimates in regional and global observed temperature changes: A new dataset from 1850. *J. Geophys. Res.,* **111,** D12106, doi:10.1029/2005JD006548.

Cess, R. D., 1976: Climate change: An appraisal of atmospheric feedback mechanisms employing zonal climatology. *J. Atmos. Sci.,* **33,** 1831–1843.

Chen, J., A. D. Del Genio, B. E. Carlson, and M. G. Bosilovich, 2008: The spatiotemporal structure of twentieth-century climate variations in observations and reanalyses. Part I: Long-term trend. *J. Climate,* **21,** 2611–2633.

Compo, G. P., and P. D. Sardeshmukh, 2008: Ocean influences on recent continental warming. *Climate Dyn.,* **32,** doi:10.1007/s00382-008-0448-9.

Forest, C. E., and R. W. Reynolds, 2008: Hot questions of temperature bias. *Nature,* **453,** 601–602.

Forster, P. F., and J. M. Gregory, 2006: Climate sensitivity and its components diagnosed from earth radiation budget data. *J. Climate,* **19,** 39–52.

Hansen, J., G. Russell, A. Lacis, I. Fung, D. Rind, and P. Stone, 1985: Climate response times—Dependence on climate sensitivity and ocean mixing. *Science,* **229,** 857–859, doi:10.1126/science.229.4716.857.

——, and Coauthors, 2005: Efficacy of climate forcings. *J. Geophys. Res.,* **110,** D18104, doi:10.1029/2005JD005776.

Hasselman, K., 1976: Stochastic climate models. I. Theory. *Tellus,* **28,** 473–485.

Hegerl, G. C., T. J. Crowley, S. K. Baum, K.-Y. Kim, and W. T. Hyde, 2003: Detection of volcanic, solar, and greenhouse gas signals in paleo-reconstructions of Northern Hemispheric temperature. *Geophys. Res. Lett.,* **30,** 1242, doi:10.1029/2002GL016635.

——, and Coauthors, 2007: Understanding and attributing climate change. *Climate Change 2007: The Physical Science Basis,* S. Solomon et al., Eds., Cambridge University Press, 663–745.

Hoerling, M., A. Kumar, J. Eishcheid, and B. Jha, 2008: What is causing the variability in global mean land temperature? *Geophys. Res. Lett.,* **35,** 1242, doi:10.1029/2008GL035984.

Hurrell, J. W., 1995: Decadal trends in the North Atlantic Oscillation: Regional temperatures and precipitation. *Science,* **269,** 676–679.

——, 1996: Influence of variations in extratropical wintertime teleconnections on Northern Hemisphere temperatures. *Geophys. Res. Lett.,* **23,** 665–668.

Jones, P. D., 1988: The influence of ENSO on global temperatures. *Climate Monitor,* **17,** 80–89.

——, A. Moberg, T. J. Osborn, and K. R. Briffa, 2003: Surface climate responses to explosive volcanic eruptions seen in long European temperature records and mid-to-high latitude tree-ring density around the Northern Hemisphere. *Volcanism and the Earth's Atmosphere,* A. Robock and C. Oppenheimer, Eds., Amer. Geophys. Union, 239–254.

Kelly, P. M., and P. D. Jones, 1996: Removal of the El Niño–Southern Oscillation signal from the gridded surface air temperature data set. *J. Geophys. Res.,* **101,** 19 013–19 022.

Knutti, R., S. Krahenmann, D. J. Frame, and M. R. Allen, 2008: Comment on "Heat capacity, time constant, and sensitivity of Earth's climate system" by S. E. Schwartz *J. Geophys. Res.,* **113,** D15103, doi:10.1029/2007JD009473.

Mass, C. F., and D. A. Portman, 1989: Major volcanic eruptions and climate: A critical evaluation. *J. Climate,* **2,** 566–593.

Nicholls, N., B. Lavery, C. Frederiksen, W. Drosdowsky, and S. Torok, 1996: Recent apparent changes in relationships between the El Niño–Southern Oscillation and Australian rainfall and temperature. *Geophys. Res. Lett.,* **23,** 3357–3360.

Penland, C., and L. Matrosova, 2006: Studies of El Niño and interdecadal variability in tropical sea surface temperatures using a nonnormal filter. *J. Climate,* **19,** 5796–5815.

Rayner, N. A., P. Brohan, D. E. Parker, C. K. Folland, J. J. Kennedy, M. Vanicek, T. Ansell, and S. F. B. Tett, 2006: Improved analyses of changes and uncertainties in marine temperature measured in situ since the mid–nineteenth century: The HadSST2 dataset. *J. Climate,* **19,** 446–469.

Robock, A., 2000: Volcanic eruptions and climate. *Rev. Geophys.,* **38,** 191–219.

——, and J. Mao, 1992: Winter warming from large volcanic eruptions. *Geophys. Res. Lett.,* **19,** 2405–2408.

——, and ——, 1995: The volcanic signal in surface temperature observations. *J. Climate,* **8,** 1086–1103.

Santer, B. D., and Coauthors, 2001: Accounting for the effects of volcanoes and ENSO in comparisons of modeled and observed temperature trends. *J. Geophys. Res.,* **106,** 28 033–28 059.

Sato, M., J. E. Hansen, M. P. McCormick, and J. B. Pollack, 1993: Stratospheric aerosol optical depth, 1850–1990. *J. Geophys. Res.,* **98** (D12), 22 987–22 994.

Solomon, S., and Coauthors, 2007: Technical summary. *Climate Change 2007: The Physical Science Basis,* S. Solomon et al. Eds., Cambridge University Press, 25–93.

Stenchikov, G. L., I. Kirchner, A. Robock, H.-F. Graf, J. C. Antuña, R. G. Grainger, A. Lambert, and L. Thomason, 1998: Radiative forcing from the 1991 Mount Pinatubo volcanic eruption. *J. Geophys. Res.,* **103,** 13 837–13 857.

Thompson, D. W. J., J. M. Wallace, and G. C. Hegerl, 2000: Annular modes in the extratropical circulation. Part II: Trends. *J. Climate,* **13,** 1018–1036.

——, J. J. Kennedy, J. M. Wallace, and P. D. Jones, 2008: A large discontinuity in the mid-twentieth century in observed global-mean surface temperature. *Nature,* **453,** 646–649, doi:10.1038/nature06982.

Trenberth, K. E., and D. A. Paolino, Jr., 1980: The Northern Hemisphere sea-level pressure data set: Trends, errors and discontinuities. *Mon. Wea. Rev.,* **108,** 855–872.

——, and D. J. Shea, 2005: Relationships between precipitation and surface temperature. *Geophys. Res. Lett.,* **32,** L14703, doi:10.1029/2005GL022760.

——, J. M. Caron, D. P. Stepaniak, and S. Worley, 2002: Evolution of El Niño–Southern Oscillation and global atmospheric surface temperatures. *J. Geophys. Res.,* **107,** 4065, doi:10.1029/2000JD000298.

Wallace, J. M., Y. Zhang, and J. A. Renwick, 1995: Dynamic contribution to hemispheric mean temperature trends. *Science,* **270,** 780–783.

Wigley, T. M. L., 2000: ENSO, volcanoes and record-breaking temperatures. *Geophys. Res. Lett.,* **27,** 4101–4104.

Worley, S. J., S. D. Woodruff, R. W. Reynolds, S. J. Lubker, and N. Lott, 2005: ICOADS release 2.1 data and products. *Int. J. Climatol.,* **25,** 823–842.

Yang, F., and M. Schlesinger, 2001: Identification and separation of Mount Pinatubo and El Niño–Southern Oscillation land sur-face temperature anomalies. *J. Geophys. Res.,* **106** (D14), 14 757–14 770.

Yulaeva, E., and J. M. Wallace, 1994: The signature of ENSO in global temperature and precipitation fields derived from the microwave sounding unit. *J. Climate,* **7,** 1719–1736.

Zhang, R., T. L. Delworth, and I. M. Held, 2007: Can the Atlantic Ocean drive the observed multidecadal variability in Northern Hemisphere mean temperature? *Geophys. Res. Lett.,* **34,** L02709, doi:10.1029/2006GL028683.